



# 1 **NAQPMS-PDAF v2.0: A Novel Hybrid Nonlinear Data Assimilation** 2 **System for Improved Simulation of PM<sub>2.5</sub> Chemical Components**

3 Hongyi Li<sup>1,3</sup>, Ting Yang<sup>1</sup>, Lars Nerger<sup>4</sup>, Dawei Zhang<sup>2</sup>, Di Zhang<sup>2</sup>, Guigang Tang<sup>2</sup>, Haibo Wang<sup>1</sup>, Yele  
4 Sun<sup>1,3</sup>, Pingqing Fu<sup>5</sup>, Hang Su<sup>1,6</sup>, Zifa Wang<sup>1,3</sup>

5 <sup>1</sup>State Key Laboratory of Atmospheric Boundary Layer Physics and Atmospheric Chemistry (LAPC), Institute of Atmospheric  
6 Physics, Chinese Academy of Sciences, Beijing 100029, China.

7 <sup>2</sup>China National Environmental Monitoring Centre, Beijing, China

8 <sup>3</sup>College of Earth and Planetary Sciences, University of Chinese Academy of Sciences, Beijing 100049, China

9 <sup>4</sup>Alfred Wegener Institute, Helmholtz Center for Polar und Marine Research, Bremerhaven, Germany

10 <sup>5</sup>Institute of Surface-Earth System Science, School of Earth System Science, Tianjin University, Tianjin 300072, China

11 <sup>6</sup>Max Planck Institute for Chemistry, Mainz, Germany

12 *Correspondence to:* Ting Yang (tingyang@mail.iap.ac.cn)

13 **Abstract.** PM<sub>2.5</sub>, a complex mixture with diverse chemical components, exerts significant impacts on the environment, human  
14 health, and climate change. However, precisely describing spatiotemporal variations of PM<sub>2.5</sub> chemical components remains a  
15 difficulty. In our earlier work, we developed an aerosol extinction coefficient data assimilation (DA) system (NAQPMS-PDAF  
16 v1.0) that is suboptimal for chemical components. This paper introduces a novel hybrid nonlinear chemical DA system  
17 (NAQPMS-PDAF v2.0) to accurately interpret key chemical components (SO<sub>4</sub><sup>2-</sup>, NO<sub>3</sub><sup>-</sup>, NH<sub>4</sub><sup>+</sup>, OC, and EC). NAQPMS-PDAF  
18 v2.0 improves upon v1.0 by effectively handling and balancing stability and nonlinearity in chemical DA, which is achieved  
19 by incorporating the non-Gaussian-distribution ensemble perturbation and hybrid Localized Kalman-Nonlinear Ensemble  
20 Transform Filter with an adaptive forgetting factor for the first time. The dependence tests demonstrate that NAQPMS-PDAF  
21 v2.0 provides excellent DA results with a minimal ensemble size of 10, surpassing previous reports and v1.0. A one-month  
22 DA experiment shows that the analysis field generated by NAQPMS-PDAF v2.0 is in good agreement with observations,  
23 especially reducing the underestimation of NH<sub>4</sub><sup>+</sup> and NO<sub>3</sub><sup>-</sup> and the overestimation of SO<sub>4</sub><sup>2-</sup>, OC, and EC. In particular, the  
24 CORR values for NO<sub>3</sub><sup>-</sup>, OC, and EC are above 0.96, and R<sup>2</sup> values are above 0.93. NAQPMS-PDAF v2.0 also demonstrates  
25 superior spatiotemporal interpretation, with most DA sites showing improvements of over 50%-200% in CORR and over 50%-  
26 90% in RMSE for the five chemical components. Compared to the poor performance in global reanalysis dataset (CORR:  
27 0.42-0.55, RMSE: 4.51-12.27 μg/m<sup>3</sup>) and NAQPMS-PDAF v1.0 (CORR: 0.35-0.98, RMSE: 2.46-15.50 μg/m<sup>3</sup>), NAQPMS-  
28 PDAF v2.0 has the highest CORR of 0.86-0.99 and the lowest RMSE of 0.14-3.18 μg/m<sup>3</sup>. The uncertainties in ensemble DA  
29 are also examined, further highlighting the potential of NAQPMS-PDAF v2.0 for advancing aerosol chemical component  
30 studies.



## 31 **1 Introduction**

32 PM<sub>2.5</sub> is a complex mixture of various chemical fractions, mainly including sulfate (SO<sub>4</sub><sup>2-</sup>), nitrate (NO<sub>3</sub><sup>-</sup>), ammonium (NH<sub>4</sub><sup>+</sup>),  
33 organic carbon (OC), and elemental carbon (EC), which diversely influences the atmospheric environment (Khanna et al.,  
34 2018), human health (Bell et al., 2007; Schlesinger, 2007; Li et al., 2022a; Alves et al., 2023), and climate change (Schult et  
35 al., 1997; Park et al., 2014; Wilcox et al., 2016). However, current detection technologies, such as field observation with in-  
36 situ sampling and chemical analysis (Zhang et al., 2015; Ming et al., 2017), remote-sensing inversion (Nishizawa et al., 2008;  
37 Nishizawa et al., 2011; Nishizawa et al., 2017), and machine learning (Lin et al., 2022; Su Lee et al., 2023) are insufficient in  
38 interpreting PM<sub>2.5</sub> chemical components due to the spatiotemporal discontinuity and limited chemical species. Although  
39 atmospheric chemistry transport models (CTMs) (Wang et al., 2014; Wang et al., 2015; Jia et al., 2017; Yang et al., 2019; Li  
40 et al., 2020; Lv et al., 2020) are commonly used to characterize spatiotemporal distribution of multiple chemical species, CTMs  
41 are associated with uncertainties in initial-boundary conditions, physiochemical mechanisms, emission inventories, and  
42 meteorological fields (Sax and Isakov, 2003; Mallet and Sportisse, 2006; Rodriguez et al., 2007; Chang et al., 2015; Miao et  
43 al., 2020; Xie et al., 2022), resulting in biases relative to real situation.

44

45 Data assimilation (DA) offers a solution to integrate the multi-source observations, CTMs, and their uncertainties effectively  
46 to enhance the simulation and forecasting capabilities of CTMs. Variational methods (3D-Var/4D-Var) (Talagrand and Courtier,  
47 1987), Ensemble Kalman Filter (EnKF) (Evensen, 1994; Evensen, 2003), EnKF-variants (EnKFs) (Bishop et al., 2001; Tippett  
48 et al., 2003; Hunt et al., 2007; Nerger et al., 2012), and hybrid EnKF-Var methods (Hamill and Snyder, 2000; Schwartz et al.,  
49 2014) are most widely applied in DA. However, variational methods have a flow-independent Background Error Covariance  
50 (BEC) with the assumption of isotropic, static, and uniform characteristics, and they need to develop the tangent linear adjoint  
51 model, which is difficult to practice for complex models. Although EnKFs and hybrid EnKF-Var methods have a flow-  
52 dependent BEC, they are sensitive to inadequate ensemble sampling and have high computational costs. Importantly, these  
53 methods cannot address model nonlinearity and non-Gaussian error distribution, yielding suboptimal results for DA in highly  
54 nonlinear CTMs.

55

56 Currently, nonlinear filters, such as Particle Filter (PF) (Gordon et al., 1993) and Nonlinear Ensemble Transform Filter (NETF)  
57 (Tödter and Ahrens, 2015), have been proposed to approximate the complete posterior probability distribution of model states  
58 and provide a better representation of non-Gaussian information based on Monte Carlo random sampling and Bayesian theory.  
59 However, PF is unstable and susceptible to filter degeneration compared to EnKFs. In a recent study, Nerger (2022) proposed  
60 the hybrid Kalman-Nonlinear Ensemble Transform Filter (KNETF) to achieve excellent DA performance in the Lorenz-63 and  
61 Lorenz-96 model with a smaller ensemble size, which combines the stability of EnKFs and the nonlinearity of NETF (Nerger,



62 2022). However, to the author's knowledge, this algorithm has not been applied to the chemical DA of CTMs.  
63  
64 Studies on chemical DA involve the assimilation of aerosol optical properties, such as aerosol optical depth (AOD) and  
65 extinction coefficient (EXT), and the particulate matters (PMs), such as the mass concentrations of PM<sub>2.5</sub> and PM<sub>10</sub>. The  
66 commonly AOD observations for DA include OMI-AOD (Ali et al., 2013), MODIS-AOD (Zhang et al., 2008; Huneus et al.,  
67 2012; Huneus et al., 2013; Rubin and Collins, 2014; Lynch et al., 2016; Werner et al., 2019; Kumar et al., 2020), AERONET-  
68 AOD (Schutgens et al., 2010; Li et al., 2016), Sun-Sky Photometer-Multiband AOD (Chang et al., 2021), GOCI-AOD (Saide  
69 et al., 2014; Luo et al., 2020; Kim et al., 2021), and Fengyun/Himawari8-AOD (Bao et al., 2019; Jin et al., 2019; Xia et al.,  
70 2019; Xia et al., 2020). These studies indicated that AOD observations can enhance the accuracy of aerosol simulation and  
71 forecast. Compared to AOD, EXT DA effectively improves the interpretation of aerosol vertical distribution (Zhang et al.,  
72 2014; Cheng et al., 2019; Wang et al., 2022). Additionally, the simultaneous DA of aerosol optical properties and PMs is widely  
73 applied in aerosol studies (Tang et al., 2015; Chai et al., 2017). According to our literature review (Yang et al., 2023), there is  
74 currently no DA study on aerosol chemical components due to the limited DA influence of PMs and AOD on chemical  
75 compositions (Chang et al., 2021) and the limited chemical observations with an extensive spatial range. Moreover, the aerosol  
76 chemical components exhibit nonlinearity and a non-Gaussian distribution (Ha, 2022), while current main-stream algorithms,  
77 such as variational methods or EnKFs, are suboptimal for chemical component DA.  
78  
79 In our previous work, we developed an aerosol vertical DA system (NAQPMS-PDAF v1.0) based on EnKFs to improve the  
80 simulation of the extinction coefficient vertical profile (Wang et al., 2022). In this study, we present a novel hybrid nonlinear  
81 DA system (NAQPMS-PDAF v2.0) towards various PM<sub>2.5</sub> chemical components through online integration of Parallel Data  
82 Assimilation Framework (PDAF, version 2.1, released on February 21<sup>st</sup>, 2023), Observation Module Infrastructure (OMI) and  
83 Nested Air Quality Prediction Model System (NAQPMS). We collected 1-month hourly surface observations of five PM<sub>2.5</sub>  
84 chemical components (NH<sub>4</sub><sup>+</sup>, SO<sub>4</sub><sup>2-</sup>, NO<sub>3</sub><sup>-</sup>, OC, and EC) over Northern China and surrounding areas. We utilized the hybrid  
85 Localized Kalman-Nonlinear Ensemble Transform Filter (LKNETF) to generate a high-resolution and high-accuracy  
86 reanalysis dataset of PM<sub>2.5</sub> chemical components for the first time. Notably, the ensemble members in NAQPMS-PDAF v2.0  
87 are generated by perturbing emission species based on their uncertainties and non-Gaussian distribution assumption. Section  
88 2 briefly introduces NAQPMS and PDAF v2.1 with OMI, respectively, and details the development of NAQPMS-PDAF v2.0,  
89 including system structure, configuration, ensemble generation, and LKNETF algorithm. The data used in this study and  
90 experimental settings are also described in Section 2. Section 3 presents the DA results, including evaluating dependencies,  
91 performance, and external comparisons. Besides, Section 3 discusses the ensemble DA uncertainty. Section 4 summarizes the  
92 conclusions and outlook.



93 **2 Method and data**

94 **2.1 NAQPMS**

95 The Nested Air Quality Prediction Modeling System (NAQPMS), developed by the Institute of Atmospheric Physics  
96 (IAP), Chinese Academy of Sciences (CAS), is used to provide background fields of key aerosol chemical components in this  
97 study. NAQPMS is capable of characterizing the three-dimensional spatiotemporal distribution of various atmospheric  
98 compositions at global and regional scales through multiple physicochemical processes (shown in Table S1) and has been  
99 widely used in atmospheric pollution and chemistry research, such as O<sub>3</sub> pollution, haze episodes (Wang et al., 2014; Du et al.,  
100 2021), regional transport (Wang et al., 2017; Wang et al., 2019), source identification (Li et al., 2022b), air quality simulation  
101 at global scale (Ye et al., 2021) and at urban-street scale (Wang et al., 2023), and acid deposition (Ge et al., 2014).

102 **2.2 PDAF v2.1 with OMI**

103 The Parallel Data Assimilation Framework (PDAF, <https://pdaf.awi.de/trac/wiki>) is an open-source and high-expandability  
104 software developed by the Alfred Wegener Institute (AWI) in Germany to integrate observations, numerical models, and  
105 assimilation systems for DA tasks, widely applied in meteorology, oceanography, land surface and atmospheric chemistry  
106 (Kurtz et al., 2016; Nerger et al., 2020; Mingari et al., 2022; Strebel et al., 2022; Wang et al., 2022; Yu et al., 2022). The initial  
107 version of PDAF (PDAF v1.0) was released in 2004. It has undergone continuous improvements and updates, with major  
108 updates including the introduction of Ensemble Transform Kalman Filter (ETKF) and its localized variant (LETKF) in version  
109 1.6, the implementation of PDAF-OMI (Observation Module Infrastructure) in version 1.16, the integration of 3D-Var methods  
110 in version 2.0, and the incorporation of the hybrid KNETF and its localized variant (LKNETF) for the first time in version 2.1,  
111 which was released in 2023 to handle the complex DA situations, such as the nonlinearity of system and non-Gaussian error  
112 distribution of model state. Notably, the version of PDAF coupled in NAQPMS-PDAF v1.0 is PDAF v1.15 (released in 2019),  
113 implying that NAQPMS-PDAF v1.0 has more limited applicability and functionality. In this work, the PDAF v2.1 is coupled  
114 in NAQPMS-PDAF v2.0.

115

116 PDAF has two modes, namely offline and online mode. For the offline mode, PDAF and the model perform separately without  
117 coupling, which is easy to write code. For the online mode, PDAF is coupled with the model, and model calculation and data  
118 assimilation perform continuously. Compared to the offline mode, the online coupling has several advantages. Firstly, the  
119 initialization process of PDAF and the model only needs to be executed once instead of twice independently. Secondly, the  
120 model integration result can be directly passed to PDAF for data assimilation. Additionally, the assimilation result of PDAF  
121 can be directly passed to the model for the next model integration. This eliminates the need for intermediate steps and improves  
122 efficiency. Thirdly, the online mode is controlled by a main program, which allows for efficient use of several processors in



123 the high-performance computing cluster. Conversely, in the offline mode, the PDAF and the model are managed by distinct  
124 programs, often with a reduced number of processors available for each program. Therefore, the online-mode PDAF is used  
125 in this study.

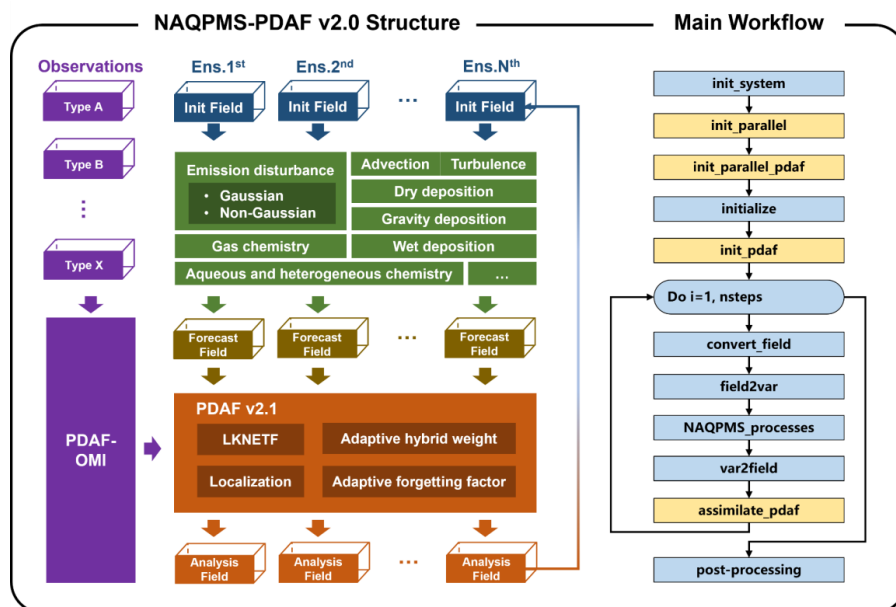
126

127 PDAF-OMI, an extension of PDAF, provides I/O interfaces for multi-type observations, simplifying user observation handling  
128 by offering generic PDAF-OMI core routines and independent user-supplied routines for each observational type. The user-  
129 supplied routines, namely *init\_dim\_obs/init\_dim\_obs\_l*, *obs\_op*, and *localize\_covar*, are responsible for reading and writing  
130 multi-type observations, applying corresponding observation operators, and performing covariance localization, respectively.  
131 The modules for all observation types are integrated into the *callback\_obs\_pdafomi*, allowing free combinations between  
132 different observation types without interference and facilitating the collaborative DA for various aerosol chemical components.  
133 PDAF-OMI was not applied in NAQPMS-PDAF v1.0. Consequently, NAQPMS-PDAF v1.0 cannot switch between different  
134 observational type combinations, and users need to define complete routines for each observation type for the DA process,  
135 resulting in more tedious code writing and higher computational costs in NAQPMS-PDAF v1.0.

## 136 **2.3 NAQPMS-PDAF v2.0**

### 137 **2.3.1 Structure of NAQPMS-PDAF v2.0**

138 Figure 1 illustrates the structure and main workflow of NAQPMS-PDAF v2.0. The observational part involves multi-type  
139 observations and PDAF-OMI. PDAF-OMI enables the simultaneous access and scheduling of multi-type and multi-source  
140 data through observational indices, which allows for flexible combination. The ensemble forecast/background fields are  
141 generated by perturbing emission species (see Sect. 2.3.3) and NAQPMS calculations (the green part in Fig. 1). Then chemical  
142 DA is performed by a novel hybrid localized nonlinear DA algorithm (LKNETF, see Sect. 2.3.4) with an adaptive hybrid  
143 weight and an adaptive forgetting factor to generate analysis/initial fields for the next realization.



144  
 145 **Figure 1: The structure of NAQPMS-PDAF v2.0**

146 NAQPMS-PDAF v2.0 implements an online coupling between NAQPMS and PDAF v2.1 with OMI, utilizing a level-2  
 147 parallel computational framework. The online coupling ensures the continuous operation of model forecasts and assimilation  
 148 analysis at each time step, achieved by directly integrating PDAF routines into the prototype code of NAQPMS (In Fig. 1 right  
 149 part, the blue represents NAQPMS main routines, while the yellow represents PDAF main routines). The level-2 parallel  
 150 computational framework, which utilizes the Message Passing Interface standard (MPI), facilitates concurrent processing and  
 151 data exchange among multiple ensemble members and parallel computation among model state matrixes within each ensemble  
 152 member, enhancing the efficiency of ensemble analysis and numerical model computations. The description of level-2 parallel  
 153 implementation was detailed in our previous work (Wang et al. 2022). The workflow of NAQPMS-PDAF v2.0 is outlined as  
 154 follows:

155 Step 1. *init\_system* module initializes NAQPMS, such as defining all model state variables, allocating numerical matrixes,  
 156 configuring parameters, I/O of meteorological fields, and emission input.

157 Step 2. *init\_parallel* module initializes MPI (MPI\_COMM\_WORLD) and model communicator (MPI\_COMM\_MODEL),  
 158 their number of processes, and the rank of a process, followed by *init\_parallel\_pdaf*, which initializes MPI communicators for  
 159 the model tasks, filter tasks and the coupling between model and filter tasks.

160 Step 3. *initialize* module initializes the target field (such as PM<sub>2.5</sub> chemical components), such as their spatiotemporal  
 161 dimensions (longitude, latitude, and time steps) and variable dimensions.

162 Step 4. *init\_pdaf* module initializes PDAF variables, such as the local state dimension, global state dimension, and settings for  
 163 analysis steps.



164 Step 5. Perform the time loop of forecast and analysis. The *convert\_field* module is employed to match the matrix storage rule  
165 of the target field between NAQPMS and PDAF to ensure compatibility. The *field2var* module collects the analysis field/initial  
166 field and establishes a relationship between the initial field/analysis field and sub-variables in NAQPMS. Subsequently, the  
167 analysis field values are allocated to the corresponding NAQPMS sub-variables, and then the *NAQPMS\_processes* module  
168 performs the forecast. After that, the *var2field* module, the inverse of the *field2var* module, assigns the NAQPMS sub-variables  
169 to the forecast field/background field. Finally, the *assimilate\_pdaf* module assimilates the target field with observations to  
170 generate an analysis field for the next iteration.

171 Step 6. post-processing is responsible for finalizing NAQPMS-PDAF, data analysis, and DA evaluation.

### 172 2.3.2 Configures

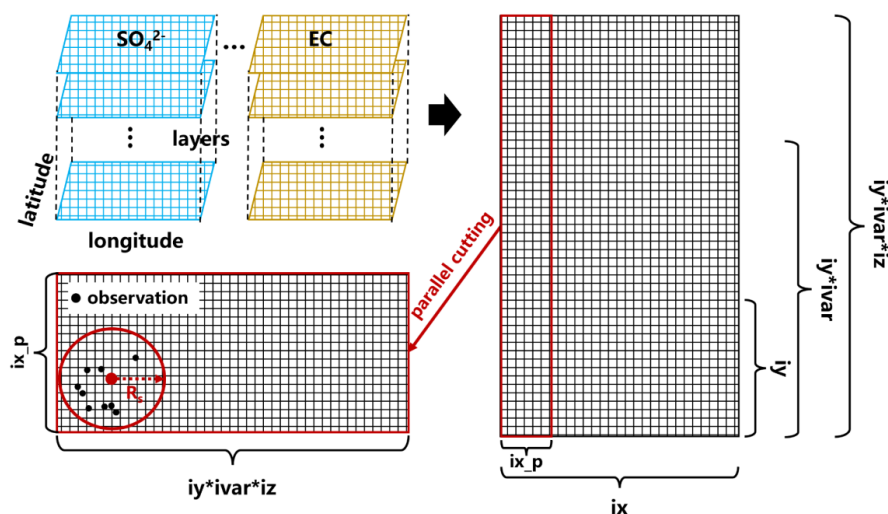
173 The meteorological field for NAQPMS is provided by the Weather Research and Forecasting model version 4.0 (WRFV4.0,  
174 <https://www.mmm.ucar.edu/models/wrf>). The initial-boundary conditions for WRF are obtained from NCEP GDAS Final  
175 Analysis (<https://rda.ucar.edu/datasets/ds083.3/>), with a horizontal resolution of  $0.25^{\circ} \times 0.25^{\circ}$  and the temporal resolution of 6  
176 hours, produced by the Global Data Assimilation System (GDAS). The land use data for WRF was updated by USGS's  
177 MCD12Q1 v006 in 2019 (<https://lpdaac.usgs.gov/products/mcd12q1v006/>) with 20 categories. Three nested model domains  
178 are conducted with the horizontal resolutions of 45 km in the East Asia region (domain1), 15 km in most areas of China except  
179 for the western area (domain2), and 5 km in the Northern China region (domain3, target research region). WRF and NAQPMS  
180 have 40 vertical layers with 27 layers within 2 km. The parameterization schemes for physical processes in WRF are shown  
181 in Table S2. The boundary condition input for NAQPMS is provided by the global chemistry transport Model for OZone And  
182 Related chemical Tracers version 2.4 (MOZART V2.4) (Horowitz et al., 2003). The anthropogenic emissions for NAQPMS  
183 are from Tsinghua University's 2016 Multi-resolution Emissions Inventory for China (MEIC, <http://www.meicmodel.org/>)  
184 with a spatial resolution of  $0.25^{\circ} \times 0.25^{\circ}$ , including residential sources, transportation sources, agricultural sources, industrial  
185 sources, and power plant sources. The computational platform is the high-performance supercomputer subsystem cluster with  
186 320 computation nodes, a total of 12,800 processors, and about 153 TB memory at the Big Data Cloud Service Infrastructure  
187 Platform (BDCSIP), which meets the demand for high-performance parallel computing of NAQPMS-PDAF v2.0.

188

189 The model state variables include  $\text{NH}_4^+$ ,  $\text{SO}_4^{2-}$ ,  $\text{NO}_3^-$ , OC, EC,  $\text{Na}^+$ , Brown carbon, soil  $\text{PM}_{2.5}$ , soil  $\text{PM}_{10}$ , sea salt, fine dust,  
190 coarse dust,  $\text{SO}_2$ ,  $\text{NO}_2$  and RH. As shown in Fig. 2, the model state has a 4-dimensional (4-D) structure, with longitudinal  
191 dimension (ix, 300 grids), latitudinal dimension (iy, 249 grids), variable dimension (ivar, 15), and vertical dimension (iz, 40  
192 layers) in that order. The 4-D model state with 15 variables is converted to a 2-D state matrix in PDAF, the number of grids in  
193 the horizontal axis direction is ix, and the number of grids in the vertical axis direction is  $iy \cdot ivar \cdot iz$ . Notably, the coordinate  
194 index of the 2-D state matrix contains 3-D information for each variable to implement the horizontal and vertical domain



195 localization separately, because the horizontal and vertical resolutions are not uniform. This structure has two advantages. First,  
 196 the parallel cutting of the horizontal axis enables the local domain to retain the full dimensional information ( $ix\_p \cdot iy \cdot ivar \cdot iz$ ,  
 197 where  $ix\_p$  is the longitudinal dimension of the local domain). Secondly, the localization in local domain permits the analysis  
 198 only executes within a small domain ( $ix\_p \cdot iy$ ) when the length of horizontal localization radius ( $R_s$ ) is smaller than  $iy$ , which  
 199 effectively reduces the influence of spurious correlations between different state variables. In this study, we set the horizontal  
 200 and vertical domain localization radius to 200 km (40 grids) and 1 layer. Besides, we further implemented the observation  
 201 localization to consider the influence of distance between analysis grid and observational grid (see Sect. 2.3.4). To minimize  
 202 computational complexity, the observation errors were assumed to be spatially isotropic, with  $0.40 \mu\text{g}/\text{m}^3$ ,  $1.00 \mu\text{g}/\text{m}^3$ ,  $0.50$   
 203  $\mu\text{g}/\text{m}^3$ ,  $3.00 \mu\text{g}/\text{m}^3$ , and  $0.50 \mu\text{g}/\text{m}^3$  for  $\text{NH}_4^+$ ,  $\text{SO}_4^{2-}$ ,  $\text{NO}_3^-$ , OC and EC, respectively.



204  
 205 **Figure 2: The structure of state variables in NAQPMS-PDAF v2.0.**

206 **2.3.3 Generation of ensemble members**

207 In ensemble DA, ensemble members interpret the uncertainty of the model or system, characterized by BEC, which  
 208 significantly impacts the DA performance (Dai et al., 2014). For CTMs, emission input directly influences the chemical  
 209 calculation and substantially contributes to the uncertainty. Perturbing emission input can effectively represent the uncertainty  
 210 in aerosol emissions and enhance the consistency of ensemble error spread, thereby improving aerosol DA (Huang et al., 2023).  
 211 CTMs are nonlinear, and model state errors are non-Gaussian distributions. To obtain non-Gaussian error distributions, we  
 212 followed Kong et al. (2021)'s method to assume that the emission errors are spatially correlated by an isotropic correlation  
 213 model with the decorrelation length of 150 km and generate perturbation coefficient matrixes with the same Gaussian  
 214 distribution as the emission species, which are subsequently transformed into non-Gaussian distribution matrixes through non-  
 215 Gaussian process generation v1.2 ([https://github.com/ECheynet/Gaussian\\_to\\_nonGaussian/](https://github.com/ECheynet/Gaussian_to_nonGaussian/)).





216

217 The target PM<sub>2.5</sub> chemical components are NH<sub>4</sub><sup>+</sup>, SO<sub>4</sub><sup>2-</sup>, NO<sub>3</sub><sup>-</sup>, OC, and EC, and the perturbed emission species correspondingly  
 218 include SO<sub>2</sub>, NO<sub>x</sub>, VOCs, NH<sub>3</sub>, CO, PM<sub>10</sub>, PM<sub>2.5</sub>, EC, and OC, with the corresponding uncertainties ( $\delta$ ) listed in Table 1. As  
 219 shown in Eq. (1), the original emission input matrix ( $E_p$ ) is multiplied by the corresponding perturbation coefficient matrix  
 220 ( $\theta_i$ ) to generate the perturbed emission input matrix ( $E_i$ ) for each emission species. The calculation of the perturbation  
 221 coefficient matrix ( $\theta_i$ ) is followed by Eq. (2)-(3). Firstly,  $N$  two-dimensional pseudorandom perturbation fields ( $P_i$ ) are created  
 222 using Evensen's method (Evensen, 1994). The uncertainties ( $\delta$ ) of the emission species are incorporated into the two-  
 223 dimensional pseudorandom perturbation fields ( $P_i$ ) to obtain the final perturbation coefficient matrixes ( $\theta_i$ ). Finally, the  
 224 Gaussian-distribution perturbation coefficient matrixes ( $\theta_i$ ) were transformed into non-Gaussian distribution coefficient  
 225 matrixes with a given target skewness (set to 1) and kurtosis (set to 6) by non-Gaussian process generation v1.2, which employs  
 226 the Moment Based Hermite Transformation Model and a cubic transformation.

227 **Table 1: The uncertainties of emission species in NAQPMS-PDAF v2.0**

| Species              | SO <sub>2</sub> | NO <sub>x</sub> | VOCs | NH <sub>3</sub> | CO   | PM <sub>10</sub> | PM <sub>2.5</sub> | EC   | OC   |
|----------------------|-----------------|-----------------|------|-----------------|------|------------------|-------------------|------|------|
| Uncertainty $\delta$ | 2.00            | 0.31            | 0.68 | 0.53            | 0.70 | 1.32             | 1.30              | 2.08 | 2.58 |

228  $E_i = E_p \times \theta_i, i = 1, 2, \dots, N$  , (1)

229  $\ln \theta_{oi} = \left( \frac{(P_i - \frac{1}{N} \times \sum_{i=1}^N P_i)}{\sqrt{\frac{1}{N} \times \sum_{i=1}^N (P_i - \frac{1}{N} \times \sum_{i=1}^N P_i)^2}} - \frac{1}{2} \times \ln(1 + \delta^2) \right) \times \sqrt{\ln(1 + \delta^2)}$  , (2)

230  $\theta_i = \frac{(\theta_{oi} - \frac{1}{N} \times \sum_{i=1}^N \theta_{oi})}{\sqrt{\frac{1}{N} \times \sum_{i=1}^N (\theta_{oi} - \frac{1}{N} \times \sum_{i=1}^N \theta_{oi})^2}} \times \left( \frac{1}{N} \times \sum_{i=1}^N \theta_{oi} \right) \times \delta + \frac{1}{N} \times \sum_{i=1}^N \theta_{oi}$  , (3)

231 Notably, all matrix operations involved are Schur Product. Where  $E_i$  denotes the  $i^{\text{th}}$  ensemble perturbed emission input matrix,  
 232  $E_p$  denotes the original unperturbed emission input matrix and  $\theta_i$  represents the  $i^{\text{th}}$  ensemble perturbation coefficient matrix.  
 233  $\theta_{oi}$  is the  $i^{\text{th}}$  ensemble original perturbation coefficient matrix, which is obtained by mathematical transformation of the  $i^{\text{th}}$   
 234 ensemble pseudorandom perturbation matrix  $P_i$ , including standardization, scaling by uncertainty ( $\delta$ ), and logarithm.

235 **2.3.4 Hybrid nonlinear DA algorithm with adaptive forgetting factor**

236 To thoroughly integrate the stability of EnKFs with the nonlinearity of nonlinear filters and be ideal for the nonlinear and non-  
 237 Gaussian-distribution situations, the hybrid LKNETF is used in this study. This section reviews the algorithms of LETKF,  
 238 LNETF, and their combination (LKNETF).

239

240 ETKF, a deterministic filter in EnKFs, efficiently obtains analysis samples using a transformation matrix and the square root  
 241 of the forecast error covariance (Bishop et al., 2001). In contrast to stochastic filters in EnKFs, ETKF prevents underestimation  
 242 of the analysis error covariance resulting from the random observation perturbations. And it is particularly applicable in  
 243 situations with small ensemble sizes (Lawson and Hansen, 2004). The realization of ETKF can be divided into the forecast



244 and analysis steps.

245

246 In the forecast step, the forecast state vector ( $\mathbf{x}_t^f$ ) at  $t$  is generated by numerical model ( $\mathbf{M}$ ) integration of the analysis state  
 247 vector ( $\mathbf{x}_{t-1}^a$ ) at  $t-1$ . The forecast error covariance matrix ( $\mathbf{P}_t^f$ ) can be calculated by the perturbation of the forecast ensemble  
 248 ( $\mathbf{X}_t^{f'}$ ).

$$249 \quad \mathbf{x}_t^f = \mathbf{M}(\mathbf{x}_{t-1}^a), \mathbf{X}_t^f = [\mathbf{x}_{1t}^f, \mathbf{x}_{2t}^f, \dots, \mathbf{x}_{Kt}^f], \quad (4)$$

$$250 \quad \mathbf{P}_t^f = \mathbf{X}_t^{f'} \mathbf{X}_t^{f' T}, \quad (5)$$

251 Where  $\mathbf{X}_t^f$  is the forecast ensemble at  $t$ , and  $K$  is the number of ensemble members.  $\mathbf{X}_t^{f'}$  is the perturbation of the forecast  
 252 ensemble at  $t$ , calculated by  $\mathbf{X}_t^f$  and the forecast ensemble mean  $\bar{\mathbf{X}}_t^f$  at  $t$ .

253

254 In the analysis step, the forecast error covariance matrix ( $\mathbf{P}_t^f$ ) at  $t$  is transformed to the analysis error covariance matrix ( $\mathbf{P}_t^a$ ) at  
 255  $t$  by a transform matrix ( $\mathbf{T}$ ).

$$256 \quad \mathbf{P}_t^a = \mathbf{X}_t^{f'} \mathbf{T} \mathbf{X}_t^{f' T}, \quad (6)$$

257 The transform matrix ( $\mathbf{T}$ ) is defined as follows and can be decomposed to a left singular vector matrix ( $\mathbf{U}$ ), a singular value  
 258 matrix ( $\mathbf{S}$ ), and a right singular vector matrix ( $\mathbf{V}$ ) through the singular value decomposition.

$$259 \quad \mathbf{T}^{-1} = \rho_{adaptive} (K - 1) \mathbf{I} + (\mathbf{H} \mathbf{X}_t^{f'})^T (\mathbf{L} \cdot \mathbf{R}^{-1}) \mathbf{H} \mathbf{X}_t^{f'} = \mathbf{U} \mathbf{S} \mathbf{V}, \quad (7)$$

$$260 \quad \rho_{adaptive} = \frac{\sigma_{ens}^2}{\sigma_{resid}^2 - \sigma_{obs}^2}, \quad (8)$$

261 Where  $\rho_{adaptive}$  is an adaptive forgetting factor, used for the inflation of error covariance estimation (the initial  $\rho_{adaptive}$  is  
 262 set to 0.9 in this study).  $\sigma_{ens}^2$  is the mean ensemble variance,  $\sigma_{resid}^2$  is mean of observation-minus-forecast residual,  $\sigma_{obs}^2$  is  
 263 mean observation variance.  $\mathbf{I}$  is the identity matrix.  $\mathbf{H}$  is the observation operator.  $\mathbf{L}$  is the localization matrix, a weight  
 264 matrix calculated by the 5<sup>th</sup>-order polynomial (Nerger, 2015), implemented in LETKF for observation localization analysis to  
 265 avoid observational spurious correlation and filter divergence effectively (Hunt et al., 2007).  $\mathbf{R}$  is the observation error  
 266 covariance matrix.

267

268 The analysis state vector ( $\mathbf{x}_t^a$ ) at  $t$  is calculated by the forecast state vector ( $\mathbf{x}_t^f$ ) at  $t$ , the perturbation of the forecast ensemble  
 269 ( $\mathbf{X}_t^{f'}$ ) at  $t$  and a weight vector ( $\mathbf{w}$ ).

$$270 \quad \mathbf{x}_t^a = \mathbf{x}_t^f + \mathbf{X}_t^{f'} \mathbf{w}, \quad (9)$$

271 The weight vector ( $\mathbf{w}$ ) is given by the following equation.



$$272 \quad \mathbf{w} = \mathbf{T}(\mathbf{H}\mathbf{X}_t^f)^T(\mathbf{L} \cdot \mathbf{R}^{-1})(\mathbf{y} - \mathbf{H}\mathbf{x}_t^f) , \quad (10)$$

273 Where  $\mathbf{y}$  is observations.

274

275 The analysis ensemble ( $\mathbf{X}_t^a$ ) at  $t$  can be obtained by forecast ensemble mean ( $\overline{\mathbf{X}}_t^f$ ) at  $t$ , the perturbation of the forecast ensemble

276 ( $\mathbf{X}_t^{f'}$ ) at  $t$  and a transform matrix ( $\mathbf{C}$ ) represented by the symmetric square root of  $\mathbf{T}$ .

$$277 \quad \mathbf{X}_t^a = \overline{\mathbf{X}}_t^f + \sqrt{\mathbf{K} - \mathbf{1}}\mathbf{X}_t^{f'}\mathbf{C} , \quad (11)$$

278 The transform matrix ( $\mathbf{C}$ ) is calculated as follows.

$$279 \quad \mathbf{C} = \mathbf{U}\mathbf{S}^{-1/2}\mathbf{U}^T , \quad (12)$$

280 NETF is a 2<sup>nd</sup>-order exact ensemble square root filter effectively applied to the nonlinear and non-Gaussian DA (Tödter and

281 Ahrens, 2015). Like PF, NETF indirectly updates the model state by using observations to affect the weights of the prior

282 ensemble. However, PF and NETF differ in the sampling method. PF utilizes the Monte Carlo and Bayesian methods to

283 calculate particle weights based on observations, which are then used to generate the analysis ensemble by weighting the

284 resampling forecast ensemble. In high-dimensional systems, as the DA progresses, the weight differences of particles increase,

285 with most particles having weights close to 0, leading to filter degeneration. In contrast, NETF generates the analysis ensemble

286 through a deterministic matrix square root transformation of the forecast ensemble, where the mean and covariance matrix of

287 the analysis ensemble match the weighted values in PF (as shown in Eq. (13)-(14)). Due to the similarity between NETF and

288 ETKF, the localization can be implemented in NETF (LNETF) (Tödter et al., 2016).

$$289 \quad \bar{\mathbf{x}}^a = \frac{1}{K}\sum_{i=1}^K \mathbf{x}_i^a = \frac{1}{K}\sum_{i=1}^K w_i \mathbf{x}_i^f , \quad (13)$$

290 Where  $\bar{\mathbf{x}}^a$  is the analysis state vector mean,  $K$  is the number of ensemble members,  $\mathbf{x}_i^a$  is the  $i^{\text{th}}$  analysis state vector,  $w_i$  is

291 the  $i^{\text{th}}$  particle weight vector in PF, which is calculated by the Bayesian method  $w_i = p(\mathbf{y}|\mathbf{x}_i^f)/p(\mathbf{y})$ ,  $\mathbf{y}$  is the observations,

292  $\mathbf{x}_i^f$  is the  $i^{\text{th}}$  forecast state vector.

$$293 \quad \mathbf{P}^a = \frac{1}{K-1}\sum_{i=1}^K (\mathbf{x}_i^a - \bar{\mathbf{x}}^a)(\mathbf{x}_i^a - \bar{\mathbf{x}}^a)^T = \sum_{i=1}^K w_i (\mathbf{x}_i^f - \bar{\mathbf{x}}^f)(\mathbf{x}_i^f - \bar{\mathbf{x}}^f)^T , \quad (14)$$

294 Where  $\mathbf{P}^a$  is the error covariance matrix of the analysis ensemble, calculated by the perturbation of the analysis ensemble.

295 In NETF,  $\mathbf{A}$  performs as a transform matrix like the transform matrix ( $\mathbf{T}$ ) in ETKF, which can be obtained from the weight

296 matrix ( $\mathbf{w}$ ).

$$297 \quad \mathbf{P}^a = \mathbf{X}^{f'}\mathbf{A}\mathbf{X}^{f'T} , \quad (15)$$

$$298 \quad \mathbf{A}^{1/2} = (\mathbf{W} - \mathbf{w}\mathbf{w}^T)^{1/2} = \mathbf{V}\mathbf{D}^{1/2}\mathbf{V}^T , \quad (16)$$



299 Where the matrix  $\mathbf{W} \equiv \text{diag}(\mathbf{w})$  is defined as a diagonal matrix created from the weight matrix ( $\mathbf{w}$ ).  $\mathbf{A}$  can be decomposed  
300 ( $\mathbf{A} = \mathbf{VDV}^T$ ) by a singular value decomposition as it is a real, symmetric, positive semidefinite matrix.  $\mathbf{V}$  is the orthogonal  
301 matrix, and  $\mathbf{D}$  is a diagonal matrix.

302

303 Then, the perturbation of the analysis ensemble ( $\mathbf{X}^{a'}$ ) and the analysis ensemble ( $\mathbf{X}^a$ ) can be obtained by applying the square  
304 root of  $\mathbf{A}$  as a transform matrix.

$$305 \mathbf{X}^{a'} = \sqrt{\mathbf{K}}\mathbf{X}^{f'}\mathbf{A}^{1/2}, \quad (17)$$

$$306 \mathbf{X}^a = \bar{\mathbf{X}}^f + \mathbf{X}^{f'}(\bar{\mathbf{W}} + \sqrt{\mathbf{K}}\mathbf{A}^{1/2}), \quad (18)$$

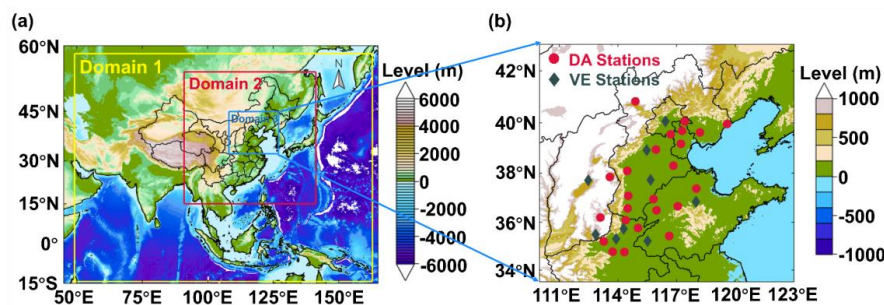
307 LKNETF combines the LETKF and LNETF through a hybrid weight  $\gamma$  to perform better in systems with different non-  
308 linearity degrees and implement in situations with smaller ensemble sizes (Nerger, 2022). When  $\gamma$  approaches 1, the analysis  
309 increment ( $\Delta\mathbf{X}_{\text{LETKF}}$ ) computed by LETKF becomes more significant and appropriate for linear systems with Gaussian  
310 distributions. Conversely, when  $\gamma$  approaches 0, the analysis increment ( $\Delta\mathbf{X}_{\text{LNETF}}$ ) computed by LNETF becomes more  
311 significant and appropriate for non-linear systems with non-Gaussian distributions. The one-step update scheme is used in this  
312 study.

$$313 \mathbf{X}_{\text{HSync}}^a = \bar{\mathbf{X}}^f + (1 - \gamma)\Delta\mathbf{X}_{\text{LNETF}} + \gamma\Delta\mathbf{X}_{\text{LETKF}}, \quad (19)$$

## 314 2.4 Data

### 315 2.4.1 Observation

316 The one-month (February 2022) hourly mass concentration observations of five  $\text{PM}_{2.5}$  chemical components ( $\text{NH}_4^+$ ,  $\text{SO}_4^{2-}$ ,  
317  $\text{NO}_3^-$ , OC, and EC) from 33 ground-based sites in Northern China and surrounding areas were collected for this work (Fig. 3).  
318 Out of the 33 sites, 24 (DA sites) were utilized for DA and internal validation, and the remaining 9 (VE sites) were used for  
319 independent verification to assess the influence of DA sites on neighboring areas. These sites were divided using the K-means  
320 clustering algorithm (Lloyd, 1982; Arthur and Vassilvitskii, 2007). The supplement provides a detailed description (Text S1).  
321  $\text{PM}_{2.5}$  hourly observations from the China National Environmental Monitoring Centre (CNEMC, <http://www.cnemc.cn/>) were  
322 employed to assess the overall mass concentration of  $\text{PM}_{2.5}$  chemical components in NAQPMS-PDAF v2.0. Due to incomplete  
323 spatial overlap between the  $\text{PM}_{2.5}$  sites and the chemical component sites, the  $\text{PM}_{2.5}$  sites were selected based on the closest  
324 coordinate Euclidean distance between  $\text{PM}_{2.5}$  sites and chemical component sites.



325

326

327

328

329

Figure 3: The model domains in WRF simulation (a) and the location of observations (b). The domain 3 in (a) is the target area in this study. Twenty-four red sites in (b) represent the sites for data assimilation, and nine green sites in (b) represent the sites for spatial independent validation. The topographic dataset is from the ETOPO1 1 arc-minute Global Relief Model, taken from the National Geophysical Data Center (Amante and Eakins, 2009).

330

#### 2.4.2 Global reanalysis dataset

331

332

333

334

335

336

337

338

339

The global reanalysis datasets of  $PM_{2.5}$  chemical components in February 2022 were obtained from the Copernicus Atmosphere Monitoring Service ReAnalysis (CAMSRA,  $0.75^\circ \times 0.75^\circ$ ) (Inness et al., 2019) and the Modern-Era Retrospective analysis for Research and Applications, Version 2 (MERRA-2,  $0.5^\circ \times 0.625^\circ$ ) (Randles et al., 2017) to compare with reanalysis dataset generated by NAQPMS-PDAF v2.0. For the consistency of data comparison, the global reanalysis surface grid data located in the observation sites of  $PM_{2.5}$  chemical component were extracted through the k-nearest neighbor search method (Friedman et al., 1977), which can efficiently match grid points and observation sites based on longitude and latitude data and Euclidean distances. Our 3-hourly NAQPMS-PDAF v2.0 output of  $NO_3^-$  and  $NH_4^+$  were extracted to compare with the CAMSRA dataset, and hourly NAQPMS-PDAF v2.0 output of  $SO_4^{2-}$ , OC, and EC were extracted to compare with MERRA-2 M2T1NXAER dataset.

340

#### 2.5 Experimental setting and evaluation method

341

342

343

344

345

346

347

348

349

350

In our study, four tests were conducted to evaluate the performance of NAQPMS-PDAF v2.0 with hourly observations of five  $PM_{2.5}$  chemical components, including (1) the dependence on ensemble size and assimilation frequency, (2) the interpretation ability on mass concentration and spatiotemporal characteristics, (3) the superiority compared to other reanalysis dataset, and (4) the uncertainty in ensemble assimilation. In practice, the ratio of ensemble size to the number of processes with 1:50 in high-performance computers was the best parallel scheme to balance computing efficiency and computing resources (Wang et al., 2022).

All the tests were run in NAQPMS-PDAF v2.0 after a spin-up experiment with 24 timesteps from 00:00 to 23:00 (LST) on February 1<sup>st</sup>, 2022. (1) For the first test, we assimilated the hourly observations of five  $PM_{2.5}$  chemical components from all sites with 48 timesteps from 00:00 (LST) on February 2<sup>nd</sup> to 23:00 (LST) on February 3<sup>rd</sup>, 2022. In the first situation, we



351 controlled a fixed assimilation frequency of 1 hour and changed the ensemble size to 2, 5, 10, 15, 20, 30, 40, and 50. In the  
352 second situation, we controlled a fixed ensemble size of 20 and changed the assimilation frequency to 1 hour, 2 hours, 3 hours,  
353 4 hours, 5 hours, 6 hours, 8 hours, and 12 hours. (2) For the second test, we set an ensemble size of 20 and an assimilation  
354 frequency of 1 h and assimilated the hourly observations of five PM<sub>2.5</sub> chemical components from DA sites with 648 timesteps  
355 from 00:00 (LST) on February 2<sup>nd</sup> to 23:00 (LST) on February 28<sup>th</sup>, 2022. We also conducted a free running (FR) experiment  
356 without assimilation in the same period for comparison. (3) For the third test, we followed the settings in the second test but  
357 assimilated the observation from all sites to generate a high-quality reanalysis dataset of five PM<sub>2.5</sub> chemical components. (4)  
358 The last test was like the first but with a different situation to investigate the impact of ensemble perturbation on ensemble  
359 assimilation. From Table 2, we fixed species uncertainty (M4 setting) with five distribution types in the first situation and fixed  
360 distribution type (T2 setting) with five SO<sub>2</sub> uncertainties in the second.

361 **Table 2: The experiment settings for emission perturbation**

| Experiment                                       | Distribution (Fixed species uncertainty) |
|--|--|
| T1   | Gaussian                                 |
| T2   | Non-Gaussian (m3=1, m4=6)                |
| T3   | Non-Gaussian (m3=-1, m4=6)               |
| T4   | Non-Gaussian (m3=1, m4=12)               |
| T5   | Non-Gaussian (m3=-1, m4=12)              |
| SO <sub>2</sub> uncertainty (Fixed distribution) |  |
| M1   | 12%                                      |
| M2   | 50%                                      |
| M3   | 100%                                     |
| M4   | 200%                                     |
| M5   | 300%                                     |

362  
363 We used the Continuous Ranked Probability Score (CRPS) to evaluate ensemble size dependency, which measures the  
364 consistency between ensemble forecast distribution and corresponding observations (Jolliffe and Stephenson, 2012). The  
365 calculation rules are referred to in Hersbach's study (Hersbach, 2000). Besides, four common statistical indicators, the Pearson  
366 correlation coefficient (CORR), root mean square error (RMSE), mean absolute error (MAE), and coefficient of determination  
367 ( $R^2$ ), were used to assess the DA system performance in interpreting PM<sub>2.5</sub> chemical components (SO<sub>4</sub><sup>2-</sup>, NO<sub>3</sub><sup>-</sup>, NH<sub>4</sub><sup>+</sup>, OC, and  
368 EC). The CORR measures the correlation between the system outputs and corresponding observations, the RMSE and MAE  
369 indicates the overall system accuracy, and the  $R^2$  reflects the proportion of variability in the observations explained by the  
370 assimilation system.



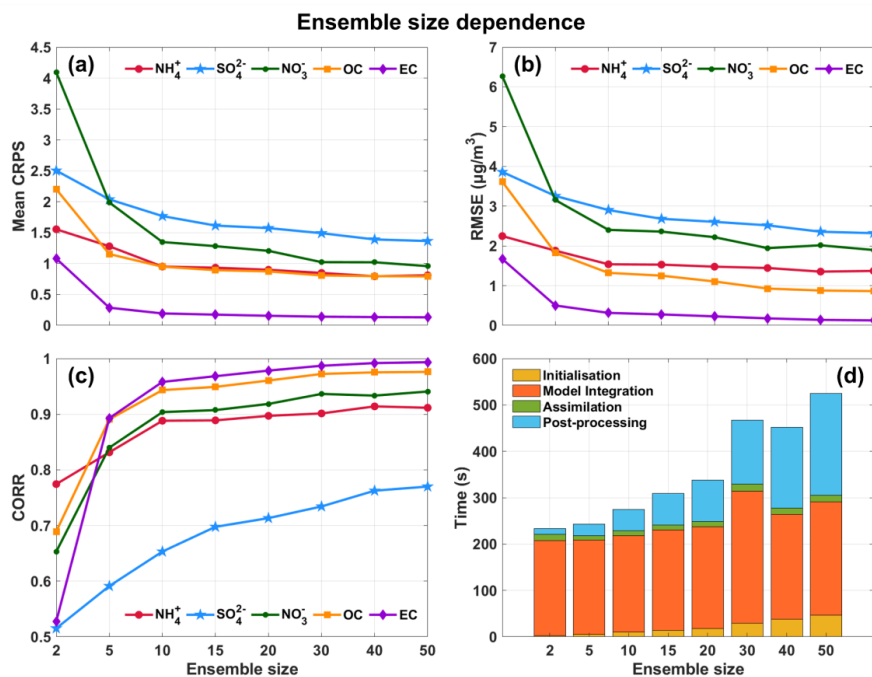
371 **3 Results and discussion**

372 **3.1 The Dependence on Ensemble Size and Assimilation Frequency for Five Components**

373 Ensemble size is a crucial parameter in ensemble assimilation, determining the model state's uncertainty range. A larger  
374 ensemble size more accurately represents the error distribution of state variables but requires considerable computing resources  
375 and time, especially for high-dimension systems. A smaller ensemble size can easily lead to underestimating the error  
376 covariance matrix, especially for the fine-resolution model (Kong et al., 2021). Thus, identifying an appropriate ensemble size  
377 to balance computational efficiency and accuracy is the primary step in ensemble DA. A prior study (NAQPMS-PDAF v1.0)  
378 only evaluated the correlation between ensemble size and parallel efficiency and concluded that the ratio of ensemble size to  
379 high-performance computing processors was 1:50 (Wang et al., 2022), while the impact of ensemble size on the accuracy and  
380 computational efficiency was neglected. In this study, we assessed the NAQPMS-PDAF v2.0 dependency on ensemble size  
381 through three statistical indicators (CRPS, RMSE, and CORR).

382

383 From Fig. 4a, when the ensemble size is at its minimum level of 2, the mean CRPS values of the five PM<sub>2.5</sub> chemical  
384 components are more significant, with NO<sub>3</sub><sup>-</sup> exhibiting the most considerable difference between the simulation distribution  
385 and observations (more than 4). With each increase in ensemble size, the mean CRPS values of the five chemical components  
386 progressively reduce and eventually reach convergence when the ensemble size is 10, implying that a hybrid nonlinear filter  
387 can maintain high accuracy and reliability in ensemble assimilation with an ensemble size that is smaller than the traditional  
388 minimum of 20 ensemble members, as observed in prior ensemble assimilation studies (Constantinescu et al., 2007; Miyazaki  
389 et al., 2012; Schwartz et al., 2014; Rubin et al., 2017; Kong et al., 2021; Tsikerdekis et al., 2021; Wang et al., 2022), including  
390 NAQPMS-PDAF v1.0. The mean CRPS value of EC is the lowest among the five chemical components, indicating the highest  
391 accuracy and reliability of EC ensemble DA. The performance of other components is similar. Like CRPS values, the values  
392 of RMSE and CORR decrease and increase, respectively, as the ensemble size increases, and convergence begins to occur  
393 when the ensemble size is 10 (Fig. 4b and c). Compared with other chemical components, the CORR value of SO<sub>4</sub><sup>2-</sup> is  
394 significantly lower, less than 0.8, possibly due to its estimated background field error covariance driven by the inadequate  
395 ensemble perturbations. Therefore, in the Discussion section, we deeply discuss the uncertainties of ensemble perturbations.



396

397

398

Figure 4: Assessment of ensemble size dependency based on mean continuous ranked probability score (CRPS) (a), root mean square error (RMSE) (b), correlation coefficient (CORR) (c), and time (d).

399

400

401

402

403

404

405

406

407

408

409

410

411

412

413

414

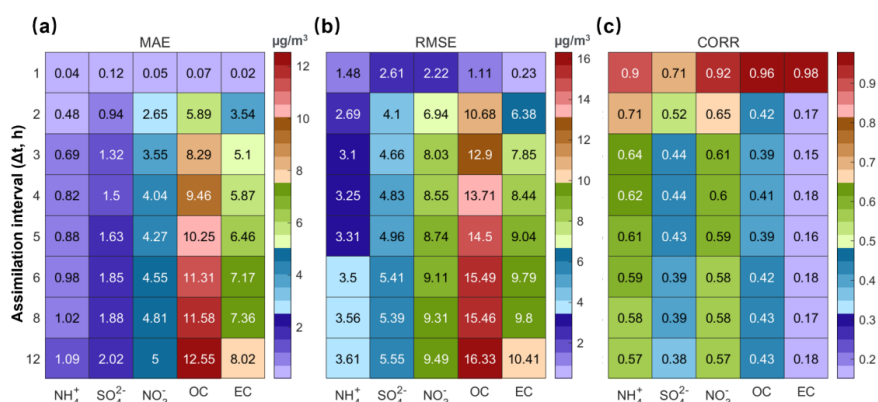
Figure 4d shows the time required for the four processes of ensemble assimilation under different ensemble sizes, including initialization, model integration, assimilation, and post-processing. The model integration process in NAQPMS-PDAF v2.0 takes the longest, followed by post-processing, initialization, and assimilation. The required time for initialization and post-processing increases with increasing ensemble size, while for model integration and assimilation, except for ensemble size 30, the required time is the same under different ensemble sizes. Generally, the time needed for ensemble sizes of 30-50 is considerably higher than that for smaller ones. Although convergence occurs with an ensemble size of 10, our work illustrates a similar time required between ensemble sizes 10 and 20. Consequently, we selected an ensemble size of 20 to ensure optimal performance of NAQPMS-PDAF v2.0, considering both assimilation efficiency and accuracy.

The assimilation frequency is the interval at which observational data is introduced into the DA system, directly affecting the practical assimilation data volume and computation cost. High-frequency DA with high-quality observations is crucial for improving numerical simulations and forecasts (Liu et al., 2021). Figure 5 demonstrates that the MAE values of the five chemical components analysis fields range from 0.02 to 0.12  $\mu\text{g}/\text{m}^3$ , RMSE values range from 0.23 to 2.61  $\mu\text{g}/\text{m}^3$ , and CORR values range from 0.71 to 0.98 at a 1-hour assimilation time interval, which is significantly better than the statistical indicators at lower assimilation frequencies. Even at a 2-hour assimilation frequency, the assimilation effect drops sharply compared to the 1-hour interval, especially for  $\text{NO}_3^-$ , OC, and EC. The values of MAE and RMSE increase by 2.6-5.82  $\mu\text{g}/\text{m}^3$  and 4.72-





415 9.57  $\mu\text{g}/\text{m}^3$ , respectively, and the CORR values decrease by 0.27-0.81. Gradual increasing trends in MAE and RMSE values  
 416 and a slight decreasing trend in CORR values are observed as assimilation frequency decreases from the 2-hour interval.  
 417 Therefore, the fast-updating assimilation with a 1-hour interval significantly improves the NAQPMS simulation. For the  
 418 forecasting field (Fig. S2), the low sensitivity of state variables to assimilation frequency suggests that NAQPMS-PDAF v2.0  
 419 can appropriately reduce assimilation frequency during the actual forecasting phase, lowering the demand for high temporal  
 420 resolution observations and computational resources.

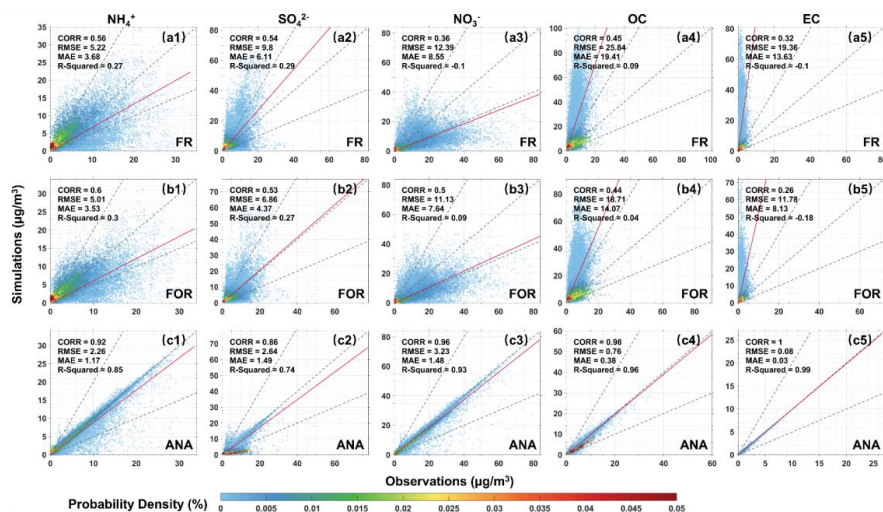


421  
 422 **Figure 5: Assessment of assimilation interval dependency based on mean absolute error (MAE) (a), root mean square error (RMSE)**  
 423 **(b), and correlation coefficient (CORR) (c) at the analysis step.**

### 424 3.2 Evaluation of NAQPMS-PDAF v2.0 performance

#### 425 3.2.1 Overall validation of DA results

426 We conducted a control experiment (free-running field, FR) without any DA and a DA experiment. This section verified the  
 427 forecast field (FOR) and analysis field (ANA) at 24 DA sites and 9 VE sites, respectively. Figure 6 shows the scatter distribution  
 428 of observations and simulations at DA sites. For FR (Fig. 6a1-a5), five chemical components have CORR values ranging from  
 429 0.32 to 0.56, and  $R^2$  values do not exceed 0.3, indicating poor consistency between observations and simulations. In detail, the  
 430 simulated mass concentrations of  $\text{SO}_4^{2-}$ , OC, and EC are significantly overestimated, while the simulated concentrations of  
 431  $\text{NH}_4^+$  and  $\text{NO}_3^-$  are underestimated. OC has the most significant error, with an RMSE value of 25.84  $\mu\text{g}/\text{m}^3$  and an MAE value  
 432 of 19.41  $\mu\text{g}/\text{m}^3$ . Besides, the error distributions of  $\text{SO}_4^{2-}$ ,  $\text{NO}_3^-$  and  $\text{NH}_4^+$  are close to a symmetric distribution with a mean  
 433 value of 0, while the error distributions of OC and EC are skewed to the left from the mean value of 0 (Fig. 7a1-a5), showing  
 434 the relatively better simulations in  $\text{SO}_4^{2-}$ ,  $\text{NO}_3^-$  and  $\text{NH}_4^+$  than in OC and EC. Overall, NAQPMS cannot interpret the mass  
 435 concentrations of the five chemical components with significant errors, mainly due to the uncertainties in chemical mechanisms  
 436 (Miao et al., 2020).



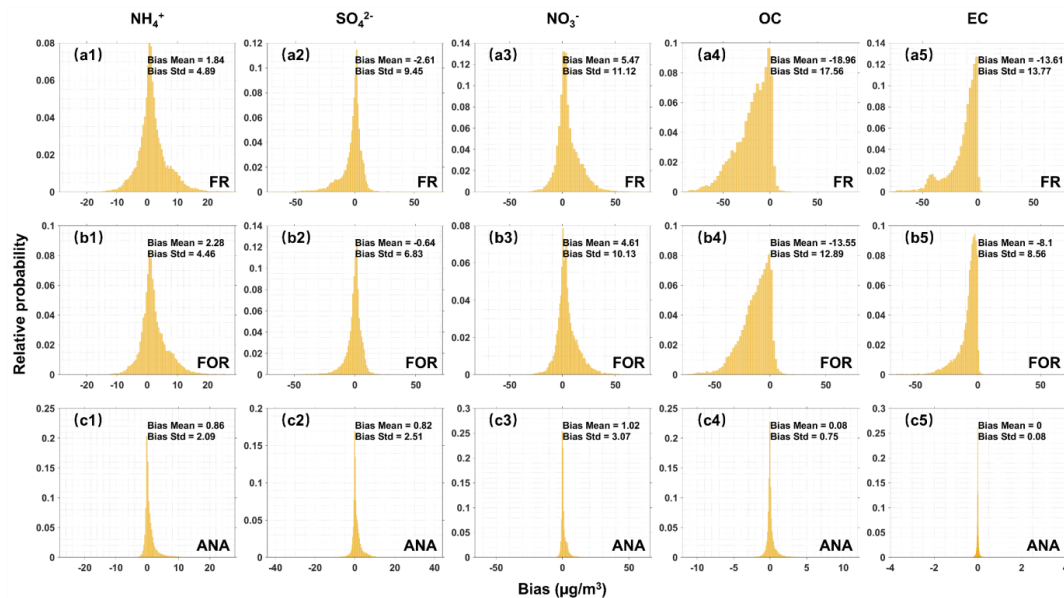
437

438

439

440

Figure 6: Scatterplots of the DA-site simulations versus the DA-site observations with probability density for the free-running field (FR, a1-a5), forecast field (FOR, b1-b5), and analysis field (ANA, c1-c5). The dotted gray lines represent the 2:1, 1:1, and 1:2 lines, and the solid red line represents the fitting regression line.



441

442

443

Figure 7: Probability distributions of bias between DA-site observations and DA-site simulations for the free-running field (FR, a1-a5), forecast field (FOR, b1-b5), and analysis field (ANA, c1-c5).

444

445

446

447

448

After DA, FOR shows a slight improvement with a slight increase in CORR and  $R^2$  and a decrease in RMSE and MAE, especially for  $\text{NH}_4^+$  and  $\text{NO}_3^-$  (Fig. 6b1-b5). Although  $\text{SO}_4^{2-}$ , OC, and EC are significantly overestimated with a slight decrease in CORR and  $R^2$ , the RMSE and MAE values decrease. Besides, the error distributions of the five chemical components are concentrated at 0, and the overestimation of OC and EC has been improved compared to FR (Fig. 7b1-b5). These results indicate that DA reduces the overall FOR errors in NAQPMS due to improved forecasting ability by obtaining optimal initial



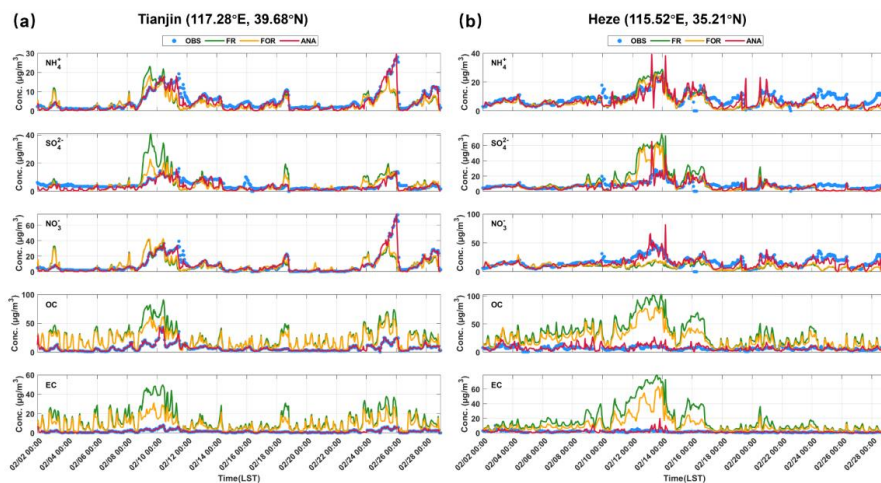
449 fields. However, further improvements are necessary to address the NAQPMS uncertainties in emission sources,  
450 meteorological input, and imperfect physiochemical mechanisms. For ANA (Fig. 6c1-c5), DA significantly improves the  
451 simulations of the five chemical components, making the ANA consistent with the observations. The CORR values are not  
452 less than 0.86, the RMSE and MAE values do not exceed  $3.23 \mu\text{g}/\text{m}^3$  and  $1.49 \mu\text{g}/\text{m}^3$ , respectively, and the  $R^2$  values are not  
453 less than 0.74. Specifically, the CORR values for  $\text{NO}_3^-$ , OC, and EC are not less than 0.96, and the  $R^2$  values are not less than  
454 0.93. The error distributions of the five chemical components concentrate to 0 with the mean bias ranging from  $0 \pm 0.08 \mu\text{g}/\text{m}^3$   
455 to  $1.02 \pm 3.07 \mu\text{g}/\text{m}^3$  (Fig. 7c1-c5). The results of VE sites show similar characteristics to the DA sites (Fig. S3 and S4).  
456 Compared to FR, the overall errors of the FOR and ANA for the five chemical components decrease with a significant  
457 improvement in ANA, showing that the CORR values of  $\text{NH}_4^+$  and  $\text{NO}_3^-$  increase by 0.15 and 0.45, respectively, the  $R^2$  values  
458 of  $\text{NH}_4^+$  and  $\text{NO}_3^-$  increase by 0.22 and 0.81, respectively, the RMSE values of OC and EC decrease by  $21.77 \mu\text{g}/\text{m}^3$  and  $17.79$   
459  $\mu\text{g}/\text{m}^3$ , respectively. Overall, the FOR and ANA errors decreased significantly. The ANA of the five chemical components at  
460 DA sites is almost entirely consistent with the observations, indicating excellent DA performance.

### 461 3.2.2 Assessment of temporal variation in chemical components

462 The ensemble DA employs a cyclic updating process wherein the forecast and analysis steps are continuously completed at  
463 each iteration (Evensen, 2003; Houtekamer and Zhang, 2016). In the forecast step, the ANA at the current time step serves as  
464 the optimal initial field to advance the model integration and obtain the FOR at the next step. In the analysis step, the FOR at  
465 the next time step provides background field information for the subsequent DA analysis to generate the ANA at the next time  
466 step. The FOR and ANA interact with each other in the temporal dimension. Therefore, in this section, we assess the ability of  
467 NAQPMS-PDAF v2.0 to interpret the temporal variations of the five chemical components. Figure 8 illustrates the time series  
468 of the five chemical components at two representative sites, including a DA site in Tianjin City and a VE site in Heze City. For  
469 the DA site (Fig. 8a), the temporal variations of  $\text{NH}_4^+$  and  $\text{NO}_3^-$  in FR and FOR exhibit better agreement with the observed  
470 temporal variations (OBS) than those of  $\text{SO}_4^{2-}$ , OC, and EC. However,  $\text{NH}_4^+$  and  $\text{NO}_3^-$  mass concentrations are significantly  
471 lower than the high-value mass concentrations observed on February 25<sup>th</sup>. The mass concentration of  $\text{SO}_4^{2-}$  in FR is greatly  
472 overestimated during the periods of Feb. 8<sup>th</sup>-11<sup>th</sup>, Feb. 18<sup>th</sup>-19<sup>th</sup>, and Feb. 24<sup>th</sup>-25<sup>th</sup>. The mass concentrations of OC and EC in  
473 FR are overestimated throughout February with substantial temporal fluctuations. Although the time series of  $\text{SO}_4^{2-}$ , OC, and  
474 EC in FOR show some improvement, noticeable differences from the OBS are still apparent. After DA, the ANA time series  
475 for the five chemical components align well with the OBS, indicating good consistency and accurate representation of temporal  
476 characteristics, such as the  $\text{NH}_4\text{NO}_3$  pollution captured on February 25<sup>th</sup>. Notably, the mass concentrations of  $\text{SO}_4^{2-}$ ,  $\text{NO}_3^-$ , and  
477  $\text{NH}_4^+$  peaked on Feb. 8<sup>th</sup>-11<sup>th</sup> and February 25<sup>th</sup>, indicating intensified atmospheric secondary chemical reactions primarily due  
478 to neutralization reactions of acidic pollutants capturing  $\text{NH}_3$ . The temporal variations of  $\text{NH}_4^+$  and  $\text{NO}_3^-$  are more similar  
479 because atmospheric  $\text{NO}_3^-$  primarily exists as  $\text{NH}_4\text{NO}_3$  rather than other metal nitrates, and  $\text{NH}_4\text{NO}_3$  can form before the

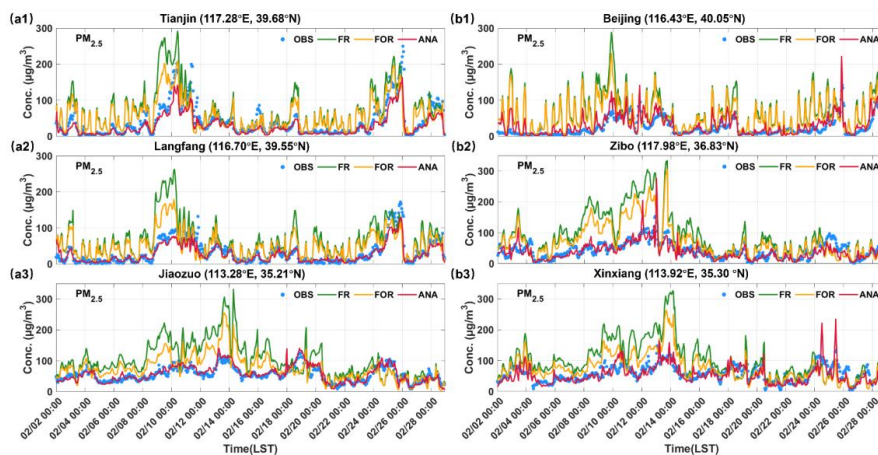


480 complete neutralization of  $\text{H}_2\text{SO}_4$  (Ge et al., 2017). The improvements at the VE site (Fig. 8b) are like those at the DA site,  
481 with the ANA time series of the five chemical components showing closer agreement with the OBS, which suggests that the  
482 localization analysis in DA effectively facilitates the propagation of observations within a specific spatial range and mitigates  
483 the assimilation anomalies caused by spurious correlations from the distant sites (Hunt et al., 2007).



484  
485 **Figure 8: Hourly variation of five  $\text{PM}_{2.5}$  chemical components in a representative DA site (a) and a representative VE site (b).**

486  $\text{NH}_4^+$ ,  $\text{SO}_4^{2-}$ ,  $\text{NO}_3^-$ , OC, and EC are critical chemical components of  $\text{PM}_{2.5}$ , and the sum of their mass concentrations can be  
487 approximated as the  $\text{PM}_{2.5}$  mass concentration. We further assessed the simulation enhancement of  $\text{PM}_{2.5}$  time series based on  
488 ground-level  $\text{PM}_{2.5}$  observations. Six representative sites were selected, including 3 DA sites (Fig. 9a1-a3) and 3 VE sites (Fig.  
489 9b1-b3). The FR and FOR in DA and VE sites show significant overestimation and poor consistency with the OBS, mainly  
490 due to the overestimation of OC and EC mass concentrations. Conversely, the  $\text{PM}_{2.5}$  time series in ANA closely matches that  
491 of the OBS, accurately capturing the actual variation of  $\text{PM}_{2.5}$ . In some specific instances, such as on February 26<sup>th</sup> at 00:00 in  
492 Tianjin City and Langfang City, the peak value of ANA was lower than that of OBS, which could be attributed to the negligence  
493 of other  $\text{PM}_{2.5}$  components (such as mineral dust and sea salt) and the inconsistency in location between ground-level  $\text{PM}_{2.5}$   
494 observational sites and chemical components observational sites. Overall, the DA of chemical component observations  
495 significantly enhanced the simulation of  $\text{PM}_{2.5}$  time series in NAQPMS. Compared to the CORR values of FR and FOR, the  
496 CORR values of ANA at the six representative sites increased by 13.64%-89.58% and 17.19%-75.00%, respectively, while the  
497 RMSE values decreased by 56.03%-83.13% and 40.74%-72.20% (Table S3).



498

499

Figure 9: Hourly variation of PM<sub>2.5</sub> in three representative DA sites (a1-a3) and three representative VE sites (b1-b3).

500

### 3.2.3 Assessment of spatial distribution in chemical components

501

DA can improve the interpretation of model states in the analysis domain by using a limited number of observations. The

502

ability to represent spatial distribution accurately is a crucial performance for aerosol DA. Figure 10 displays the spatial

503

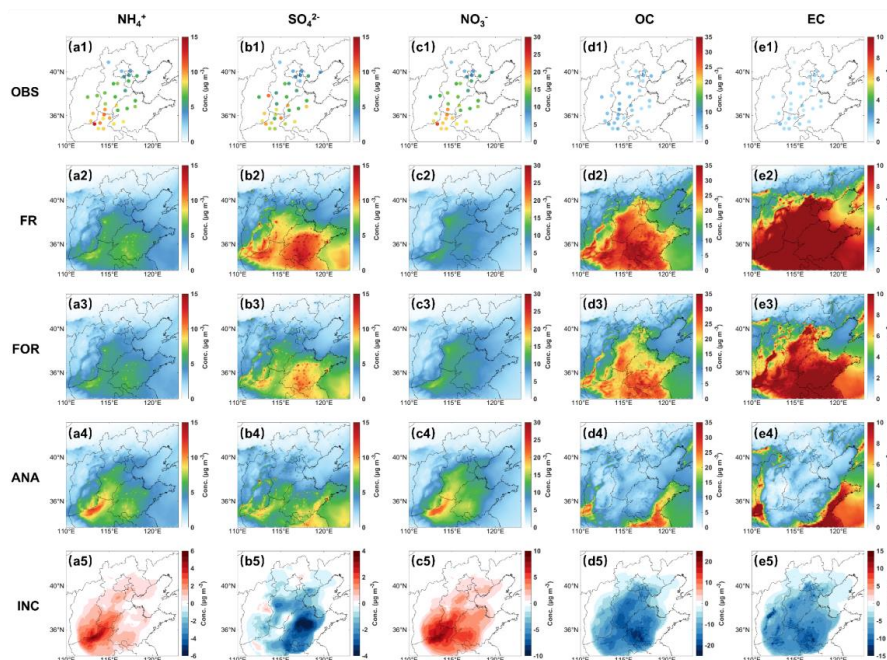
distribution of the monthly average mass concentrations for the five chemical components, including OBS, FR, FOR, ANA,

504

and analysis increment (INC). The spatial distributions of bias and statistical indicators for FR, FOR, and ANA are shown in

505

Fig. 11 and Fig. 12, respectively.

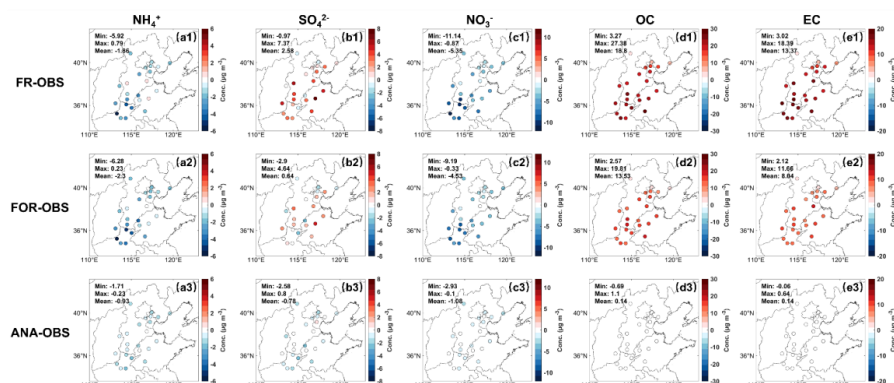


506

507

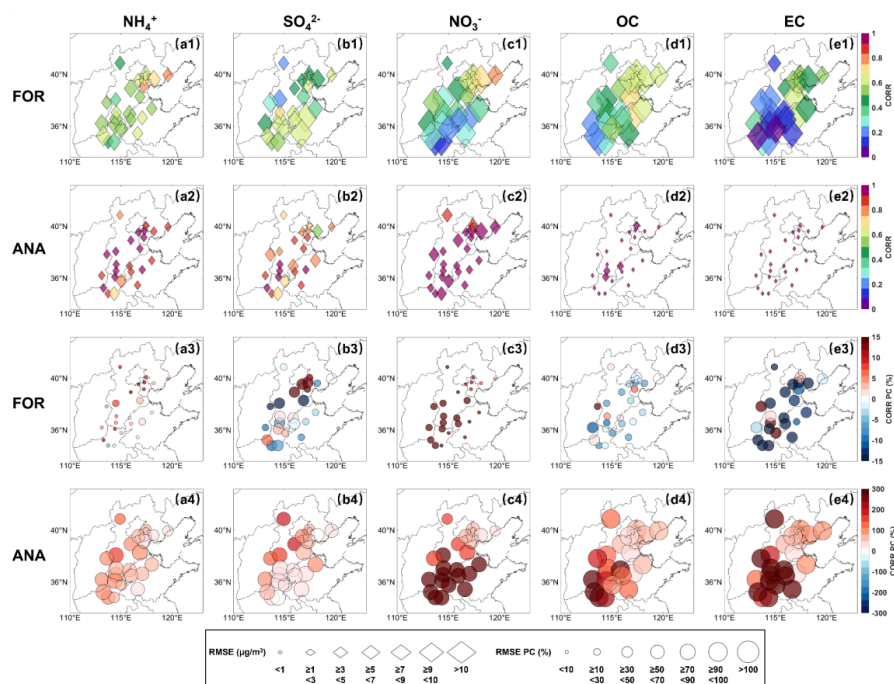
Figure 10: Spatial concentration distribution of site observation (OBS, a1-e1), free-run field (FR, a2-e2), forecast field (FOR, a3-e3), analysis field (ANA, a4-e4), and increment (INC) between ANA and FR (a5-e5) for five PM<sub>2.5</sub> chemical components.

508



509  
 510  
 511

Figure 11: Spatial distribution of DA-site bias for five PM<sub>2.5</sub> chemical components from observation (OBS) for the free-running field (FR, a1-e1), forecast field (FOR, a2-e2) and analysis field (ANA, a3-e3).



512  
 513  
 514  
 515  
 516

Figure 12: Spatial distribution of DA-site statistical indicators for five PM<sub>2.5</sub> chemical components. (a1-e1) represents the values of RMSE and CORR for the forecast field (FOR), (a2-e2) same as (a1-e1) but for analysis field (ANA), (a3-e3) represents the improvement of RMSE and CORR for the forecast field (FOR), (a4-e4) same as (a3-e3) but for analysis field (ANA). The size represents the value of RMSE in (a1-e2) and the improvement percentage compared to non-assimilation in (a3-e4), respectively.

517 The spatial characteristics of NH<sub>4</sub><sup>+</sup> and NO<sub>3</sub><sup>-</sup> are similar. Compared to the OBS (Fig. 10a1 and c1), the FR (Fig. 10a2 and c2)  
 518 and FOR (Fig. 10a3 and c3) have failed to capture the high-value mass concentrations in the border area between Hebei  
 519 province, Shanxi province, Henan province, and Shandong province, especially in the northern region of Henan province. The  
 520 primary reason is the uncertainties in emission inventories in winter heating periods, which results in insufficient emission  
 521 statistics of gaseous precursors NO<sub>x</sub> and NH<sub>3</sub> (Aleksankina et al., 2018). After DA, this situation is significantly improved



522 with the ANA (Fig. 10a4 and c4). The INCs in the Beijing-Tianjin-Hebei region, Shanxi province, Henan province, and  
523 Shandong province are positive (Fig. 10a5 and c5), indicating varying degrees of improvement in correcting the  
524 underestimation of mass concentrations. Specifically, for  $\text{NH}_4^+$  and  $\text{NO}_3^-$  at DA sites, the biases between the OBS and ANA  
525 are significantly reduced compared to the biases between the OBS and FR (Fig. 11), with the mean absolute bias decreasing  
526 by  $0.93 \mu\text{g}/\text{m}^3$  and  $4.27 \mu\text{g}/\text{m}^3$ , respectively. Moreover, the overall biases at VE sites also decrease (Fig. S5). As for the spatial  
527 statistical indicators of  $\text{NH}_4^+$  (Fig. 12a1 and a2), the CORR values in FOR and ANA range from 0.39 to 0.79 and 0.70 to 0.97,  
528 respectively, and the RMSE values range from  $3.16 \mu\text{g}/\text{m}^3$  to  $7.65 \mu\text{g}/\text{m}^3$  and  $1.20 \mu\text{g}/\text{m}^3$  to  $3.49 \mu\text{g}/\text{m}^3$ , respectively. As for  
529 the spatial statistical indicators of  $\text{NO}_3^-$  (Fig. 12c1 and c2), the CORR values in FOR and ANA range from 0.09 to 0.76 and  
530 0.89 to 0.99, respectively, and the RMSE values range from  $4.88 \mu\text{g}/\text{m}^3$  to  $15.69 \mu\text{g}/\text{m}^3$  and  $1.34 \mu\text{g}/\text{m}^3$  to  $5.39 \mu\text{g}/\text{m}^3$ ,  
531 respectively. For the FOR, the improvement in accuracy for  $\text{NO}_3^-$  is more significant than that for  $\text{NH}_4^+$ , with the CORR values  
532 of most DA sites increasing by more than 10% and the RMSE of most DA sites decreasing by not less than 10% (Fig. 12a3  
533 and c3). For the ANA,  $\text{NH}_4^+$  and  $\text{NO}_3^-$  exhibit significant improvements in CORR and RMSE, as most DA sites show over  
534 150% in CORR and over 50% in RMSE (Fig. 12a4 and c4). The improvements can also be found for  $\text{NH}_4^+$  and  $\text{NO}_3^-$  at VE  
535 sites (Fig. S6). The spatial consistency of  $\text{NH}_4^+$  and  $\text{NO}_3^-$  indicates that  $\text{NH}_4\text{NO}_3$  is the primary aerosol chemical component,  
536 highlighting the necessity of coordinated control of precursor  $\text{NO}_x$  and  $\text{NH}_3$ .

537

538 Unlike  $\text{NH}_4^+$  and  $\text{NO}_3^-$ , compared to the OBS (Fig. 10b1), the mass concentrations of  $\text{SO}_4^{2-}$  in the FR and FOR (Fig. 10b2 and  
539 b3) are significantly overestimated, especially in Shandong province. In contrast, the ANA has dramatically improved (Fig.  
540 10b4), with most areas showing negative INCs (Fig. 10b5). The mean absolute biases in DA and VE sites have decreased by  
541  $1.80 \mu\text{g}/\text{m}^3$  and  $2.68 \mu\text{g}/\text{m}^3$ , respectively (Fig. 11 and Fig. S5). Specifically, after DA, the CORR values of the FOR and ANA  
542 range from 0.22 to 0.71 and 0.58-0.97, and the RMSE values range from  $3.42 \mu\text{g}/\text{m}^3$  to  $11.07 \mu\text{g}/\text{m}^3$  and  $1.20 \mu\text{g}/\text{m}^3$  to  $4.30$   
543  $\mu\text{g}/\text{m}^3$ , respectively (Fig. 12b1 and b2). The CORR and RMSE values in FOR have significantly improved (Fig. 12b3) at DA  
544 sites around Beijing. While the CORR values in ANA have increased by more than 13%, with most DA sites showing an  
545 increase of over 50%, and RMSE values have decreased by no less than 30%, with most DA sites showing a decrease of over  
546 70% (Fig. 12b4). Besides, half of the VE sites show significant improvement in the CORR and RMSE in the FOR and ANA,  
547 mainly due to their proximity to more DA sites (Fig. S6). The OBS and ANA indicate a considerable control in  $\text{SO}_4^{2-}$  pollution  
548 during the winter heating period due to the emission reduction of gaseous precursors (Zhai et al., 2019; Yan et al., 2021).

549

550 The spatial distributions of OC and EC exhibit similarities (Fig. 10d1 and e1), consistent with the finding of a strong correlation  
551 between OC and EC in winter (Cao et al., 2007). Since the low temperature and weakened photochemical reactions in winter  
552 reduced secondary OC (SOC) generation, and primary OC (POC) and EC mainly originate from direct anthropogenic  
553 emissions, such as combustion (Guo, 2016). Compared to the OBS, the mass concentrations in FR (Fig. 10d2-d3) and FOR

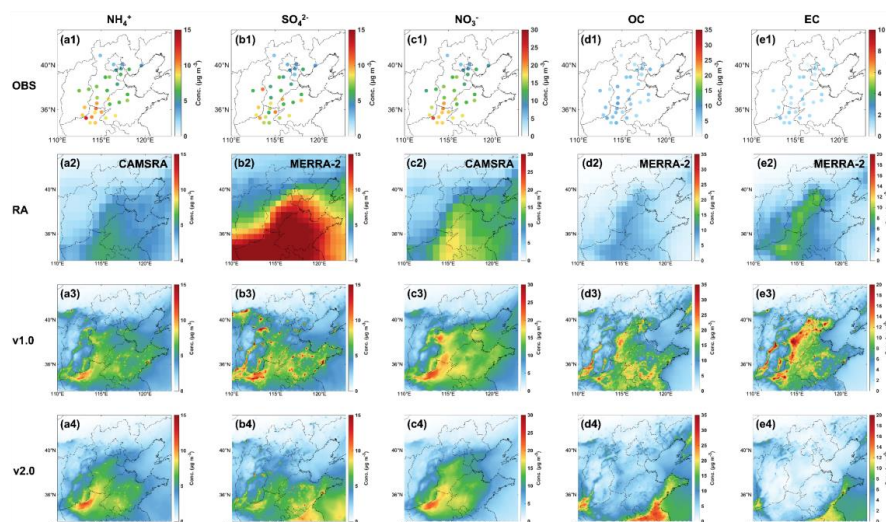


554 (Fig. 10e2-e3) are significantly overestimated over a wide range. Similar overestimations have also been reported in the global  
555 reanalysis datasets of CAMS and MERRA-2, likely attributed to the hygroscopic growth scheme of carbonaceous aerosols in  
556 the models, poorly constrained semi-volatile species escaping from primary organic aerosols (Soni et al., 2021), and aging  
557 mechanisms in the models (Huang et al., 2013). After DA, the spatial distribution of the ANA aligns entirely with that of the  
558 OBS (Fig. 10d4 and e4), with the improvements in all overestimations (Fig. 10d5 and e5) and the average biases of OC and  
559 EC at DA sites both significantly decreasing to  $0.14 \mu\text{g}/\text{m}^3$  (Fig. 11d3 and e3). The VE sites show similar results to the DA  
560 sites, with the average biases of less than  $2 \mu\text{g}/\text{m}^3$  (Fig. S5d3 and e3). Specifically, for OC (Fig. 12d1 and d2), the CORR  
561 values in FOR and ANA are 0.18-0.71 and 0.92-1.00, respectively, with RMSE values of  $7.91 \mu\text{g}/\text{m}^3$ - $26.27 \mu\text{g}/\text{m}^3$  and  $0.16$   
562  $\mu\text{g}/\text{m}^3$ - $1.45 \mu\text{g}/\text{m}^3$ , respectively. For EC (Fig. 12e1 and e2), the CORR values in FOR and ANA are 0.01-0.66 and 0.97-1.00,  
563 respectively, with RMSE values of  $5.33 \mu\text{g}/\text{m}^3$ - $16.91 \mu\text{g}/\text{m}^3$  and  $0.01 \mu\text{g}/\text{m}^3$ - $0.26 \mu\text{g}/\text{m}^3$ , respectively. Although significant  
564 improvements are not observed in FOR at some specific DA sites, the RMSE values at all DA sites decrease by 10%-50% (Fig.  
565 12d3 and e3). The CORR values of OC and EC in ANA increase by more than 30%, with most DA sites exceeding 200%, and  
566 the RMSE values decrease by more than 90% (Fig. 12d4 and e4). At VE sites (Fig. S6), significant improvements in the CORR  
567 are not observed, but the RMSE values in the FOR and ANA decrease, which indicates that DA has limited benefits for whole  
568 areas but can effectively reduce biases of whole areas.

### 569 3.3 Compared to NAQPMS-PDAF v1.0 and global reanalysis dataset

570 To comprehensively evaluate the competitiveness and superiority of NAQPMS-PDAF v2.0 in generating the reanalysis  
571 datasets of the  $\text{PM}_{2.5}$  chemical compositions, we assimilated the mass concentrations of the five  $\text{PM}_{2.5}$  chemical components  
572 from all sites (sum of DA sites and VE sites) in February 2022 to generate a reanalysis dataset. We compared our reanalysis  
573 dataset with the global reanalysis (RA) datasets (CAMSR and MERRA-2) and NAQPMS-PDAF v1.0 output. Figure 13  
574 illustrates the spatial distribution of the monthly average mass concentrations for the five chemical components. Compared to  
575 the OBS (Fig. 13a1 and c1), CAMSR underestimates the  $\text{NH}_4^+$  and  $\text{NO}_3^-$  concentrations and fails to capture the high-value  
576 concentration in northern Henan Province (Fig. 13a2 and c2). Meanwhile, MERRA-2 overestimates the concentrations of  
577  $\text{SO}_4^{2-}$ , OC, and EC (Fig. 13b2, d2 and e2), particularly  $\text{SO}_4^{2-}$ , exhibiting a large region with inaccurately high concentrations.  
578 Besides, CAMSR (approximately  $80 \times 80 \text{ km}^2$ ) and MERRA-2 ( $55 \times 70 \text{ km}^2$ ) have significantly lower spatial resolutions  
579 compared to NAQPMS-PDAF v2.0 ( $5 \times 5 \text{ km}^2$ ). Therefore, NAQPMS-PDAF v2.0 provides a more detailed description of the  
580 pollution characteristics of chemical components in Northern China and surrounding areas compared to RA.





581  
582 **Figure 13: Spatial distribution of the monthly averaged concentration of five PM<sub>2.5</sub> chemical components for observations (OBS, a1-**  
583 **e1), global reanalysis data (RA, a2-e2), NAQPMS-PDAF v1.0 analysis data (a3-e3) and NAQPMS-PDAF v2.0 analysis data (a4-e4).**

584 Although NAQPMS-PDAF v1.0 demonstrates a superior spatial representation of the five chemical components when  
585 compared to RA, it fails to capture the high-value concentrations of NH<sub>4</sub><sup>+</sup> in the northwest of Henan Province and correct the  
586 high-value concentrations of NH<sub>4</sub><sup>+</sup> in the central and western areas of Hebei Province (Fig. 13a3). Moreover, the scattered  
587 high-value concentrations of SO<sub>4</sub><sup>2-</sup> in the North China Plain do not align with the spatial characteristics of the OBS (Fig. 13b3).  
588 Notably, NAQPMS-PDAF v1.0 exhibits poor performance in interpreting OC and EC with significant overestimations in a  
589 wide range (Fig. 13d3 and e3), which indicates that NAQPMS-PDAF v1.0 is weaker than NAQPMS-PDAF v2.0 in terms of  
590 DA performance on chemical components, primarily due to insufficient propagation of observations. In NAQPMS-PDAF v2.0,  
591 the LKNETF algorithm with an adaptive forgetting factor is more suitable for the nonlinear and non-Gaussian situations  
592 compared to EnKFs in NAQPMS-PDAF v1.0, and the ensemble perturbation with non-Gaussian distribution can better  
593 represent the reasonable error distribution of model states.

594

595 Table 3 presents a quantitative comparison of three reanalysis datasets. Compared to the CORR of NAQPMS-PDAF v2.0  
596 (0.86-0.99), the CORR of RA for the five chemical components is significantly lower (0.42-0.55). Moreover, NAQPMS-PDAF  
597 v1.0 exhibits significantly poorer consistency in SO<sub>4</sub><sup>2-</sup>, OC, and EC, with CORR values ranging from 0.35 to 0.57. NAQPMS-  
598 PDAF v2.0 has lower overall RMSE values (0.14 µg/m<sup>3</sup>-3.18 µg/m<sup>3</sup>) compared to RA and NAQPMS-PDAF v1.0, with RMSE  
599 values ranging from 4.51 µg/m<sup>3</sup> to 12.27 µg/m<sup>3</sup> and 2.46 µg/m<sup>3</sup> to 15.50 µg/m<sup>3</sup>, respectively. The characteristics of the R<sup>2</sup> are  
600 like those of the CORR and RMSE. For NH<sub>4</sub><sup>+</sup> and NO<sub>3</sub><sup>-</sup>, NAQPMS-PDAF v2.0 (0.85 and 0.93) and v1.0 (0.80 and 0.96) are  
601 much higher than RA (0.09 and 0.13). Notably, for SO<sub>4</sub><sup>2-</sup>, OC, and EC, NAQPMS-PDAF v2.0 (0.74-0.98) is significantly  
602 higher than v1.0 (-0.16-0.25) and RA (-0.15-0.25). Overall, NAQPMS-PDAF v2.0 more accurately and consistently interprets



603 the five chemical components, particularly for  $\text{NH}_4^+$ ,  $\text{SO}_4^{2-}$ , OC, and EC. The reasons are summarized as follows. (1) The DA  
604 frequency of CAMSRA is 12 hours, which is lower than the hourly DA frequency in NAQPMS-PDAF v2.0. (2) CAMSRA  
605 only assimilates satellite retrievals (Inness et al., 2019), and MERRA-2 only assimilates aerosol optical depth (AOD) from  
606 both ground-based and space-based remote sensing platforms (Randles et al., 2017). The aerosol optical information analysis  
607 increment cannot be allocated to each chemical component accurately and reasonably due to the lack of a deterministic  
608 relationship between aerosol optical information and  $\text{PM}_{2.5}$  chemical components. (3) NAQPMS-PDAF v1.0 has evident DA  
609 shortcomings for chemical components due to the limited DA algorithm under the assumption of linear model or system,  
610 inappropriate ensemble perturbation under the assumption of Gaussian distribution, and inadequate observational modules. (4)  
611 The state variable structure in NAQPMS-PDAF v1.0 lacks the capacity to effectively mitigate the impact of spurious  
612 correlations between chemical component variables, even when using analytical localization.

613 **Table 3: Statistical indicators (CORR, RMSE,  $R^2$ ) of five  $\text{PM}_{2.5}$  chemical components for global reanalysis data (RA), NAQPMS-  
614 PDAF v1.0 analysis data and NAQPMS-PDAF v2.0 analysis data.**

| Components         | CORR |      |      | RMSE ( $\mu\text{g}/\text{m}^3$ ) |       |      | $R^2$ |       |      |
|--------------------|------|------|------|-----------------------------------|-------|------|-------|-------|------|
|                    | RA   | v1.0 | v2.0 | RA                                | v1.0  | v2.0 | RA    | v1.0  | v2.0 |
| $\text{NH}_4^+$    | 0.49 | 0.90 | 0.92 | 5.59                              | 2.53  | 2.22 | 0.09  | 0.80  | 0.85 |
| $\text{SO}_4^{2-}$ | 0.55 | 0.57 | 0.86 | 12.27                             | 5.45  | 2.61 | 0.25  | 0.25  | 0.74 |
| $\text{NO}_3^-$    | 0.54 | 0.98 | 0.96 | 10.27                             | 2.46  | 3.18 | 0.13  | 0.96  | 0.93 |
| OC                 | 0.50 | 0.42 | 0.97 | 4.51                              | 12.92 | 0.93 | 0.15  | -0.09 | 0.93 |
| EC                 | 0.42 | 0.35 | 0.99 | 7.59                              | 15.50 | 0.14 | -0.15 | -0.16 | 0.98 |

### 615 3.4 The uncertainty in NAQPMS-PDAF v2.0

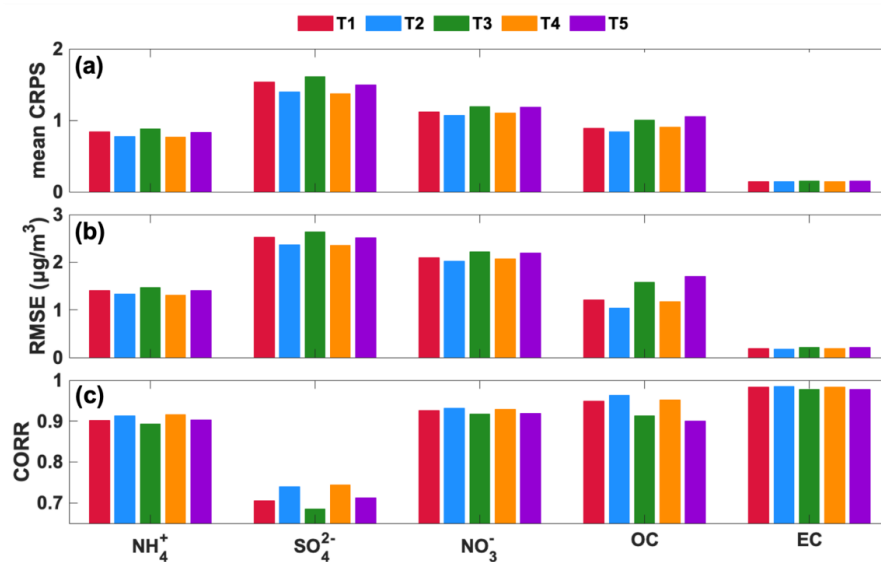
616 In ensemble DA, the ensemble members represent possible values of the model states, and the ensemble sampling can  
617 determine the uncertainties of the model states. Therefore, the ensemble generation directly affects the propagation of  
618 observations and subsequently impacts the final DA performance. Previous studies generated ensemble members based on the  
619 uncertainties of emission species and the Gaussian-distribution assumption to satisfy the requirements of EnKFs algorithms  
620 (Kong et al., 2021; Wang et al., 2022). However, the true error probability distribution of emission species is not an ideal  
621 Gaussian distribution, and the assumption will introduce errors. In this study, we coupled the hybrid nonlinear DA algorithm  
622 (LKNETF) with NAQPMS to handle the nonlinear and non-Gaussian situations, which combines the stability of LETKF with  
623 the nonlinearity of LNETF. Therefore, we evaluate the performance of ensemble members with different uncertainties and  
624 error probability distributions in NAQPMS-PDAF v2.0 through two groups of sensitivity experiments.

625

626 The first group of experiments (T1-T5) involves controlling the  $\text{SO}_2$  uncertainty as a fixed value of 200% and transforming  
627 the distribution of the perturbation coefficient matrix. The second group of experiments (M1-M5) focuses on assessing the  
628 influence of  $\text{SO}_2$  uncertainty on  $\text{NH}_4^+$  and  $\text{SO}_4^{2-}$  DA based on a fixed non-Gaussian distribution ( $m_3=1$ ,  $m_4=6$ ). Figure 14



629 shows the statistical indicators of the five chemical components under different error probability distributions, including a  
630 Gaussian distribution (T1) and four non-Gaussian distributions (T2-T5). The mean CRPS and RMSE in T2 and T4 are lower  
631 than those in T1, T3, and T5, and the CORR values in T2 and T4 are higher than those in T1, T3, and T5, indicating that the  
632 DA performance of non-Gaussian-distribution assumption is superior to that of Gaussian-distribution assumption. Moreover,  
633 positively skewed non-Gaussian distribution performs better than negatively skewed distribution. Except for  $\text{SO}_4^{2-}$ , the  
634 performance in T2 outweighs that in T4 for other chemical components, implying that higher kurtosis harms the chemical  
635 components DA.



636  
637 **Figure 14: Statistical indicators (mean CRPS (a), RMSE (b), and CORR (c)) of five  $\text{PM}_{2.5}$  chemical components for five perturb**  
638 **experiments based on distribution.**

639  $\text{SO}_2$  is a crucial precursor of  $\text{NH}_4^+$  and  $\text{SO}_4^{2-}$ , and perturbing  $\text{SO}_2$  affects the forecast and simulation of  $\text{NH}_4^+$  and  $\text{SO}_4^{2-}$ . Table  
640 4 presents statistical indicators of  $\text{NH}_4^+$  and  $\text{SO}_4^{2-}$  analysis fields based on ensemble perturbations with different  $\text{SO}_2$   
641 uncertainties (12%-300%). Increasing the uncertainty of  $\text{SO}_2$  from 12% to 200% leads to a decrease in the mean CRPS in the  
642  $\text{SO}_4^{2-}$  analysis field from 2.67 to 1.40, an increase in the CORR from 0.51 to 0.74, and a reduction in the RMSE from 4.10  
643  $\mu\text{g}/\text{m}^3$  to 2.37  $\mu\text{g}/\text{m}^3$ . Similarly, the mean CRPS in the  $\text{NH}_4^+$  analysis field decreases from 0.98 to 0.77, the CORR increases  
644 from 0.88 to 0.91, and the RMSE decreases from 1.55  $\mu\text{g}/\text{m}^3$  to 1.33  $\mu\text{g}/\text{m}^3$ . It indicates that increasing the uncertainty of  $\text{SO}_2$   
645 improves the DA performance on  $\text{NH}_4^+$  and  $\text{SO}_4^{2-}$  because the higher  $\text{SO}_2$  uncertainty makes  $\text{SO}_2$  perturbed sufficiently, and  
646 the estimated error probability distribution is closer to the real distribution, resulting in a sufficient spread of observations.  
647 However, when the uncertainty of  $\text{SO}_2$  reaches 300%, the statistical indicators do not significantly improve and even worsen  
648 because excessively high  $\text{SO}_2$  uncertainty causes the estimated error probability distribution to deviate from the true  
649 distribution. Thus, selecting appropriate uncertainties for emission species is crucial in aerosol chemical component DA.



650

651 To summarize, the non-Gaussian-distribution assumption outperforms the Gaussian-distribution assumption in NAQPMS-  
652 PDAF v2.0. Positive skewness performs better than negative skewness, and excessively high kurtosis should be avoided.  
653 Additionally, appropriately increasing the uncertainty of SO<sub>2</sub> enhances the DA performance of NH<sub>4</sub><sup>+</sup> and SO<sub>4</sub><sup>2-</sup>. Future studies  
654 should conduct more sensitivity experiments on emission species perturbation to determine the suitable schemes for different  
655 aerosol chemical components.

656 **Table 4: Statistical indicators (mean CRPS (a), RMSE (b), and CORR (c)) of five PM<sub>2.5</sub> chemical components for five perturb**  
657 **experiments based on SO<sub>2</sub> emission uncertainty.**

| Experiment | SO <sub>4</sub> <sup>2-</sup> |      |      | NH <sub>4</sub> <sup>+</sup> |      |      |
|------------|-------------------------------|------|------|------------------------------|------|------|
|            | CRPS                          | CORR | RMSE | CRPS                         | CORR | RMSE |
| M1         | 2.67                          | 0.51 | 4.10 | 0.98                         | 0.88 | 1.55 |
| M2         | 2.07                          | 0.59 | 3.24 | 0.92                         | 0.89 | 1.48 |
| M3         | 1.61                          | 0.69 | 2.63 | 0.83                         | 0.91 | 1.39 |
| M4         | 1.40                          | 0.74 | 2.37 | 0.77                         | 0.91 | 1.33 |
| M5         | 1.41                          | 0.74 | 2.39 | 0.78                         | 0.91 | 1.33 |

#### 658 4 Conclusions

659 In this paper, we online coupled NAQPMS with PDAF-OMI to develop a novel hybrid nonlinear DA system (NAQPMS-  
660 PDAF v2.0) with level-2 parallelization based on a hybrid Kalman-Nonlinear Ensemble Transform Filter (LKNETF) for the  
661 first time. Compared to NAQPMS-PDAF v1.0, NAQPMS-PDAF v2.0 with OMI can be applied with multiple component  
662 types and nonlinear/non-Gaussian situations in chemical analysis to effectively interpret five PM<sub>2.5</sub> chemical components  
663 (NH<sub>4</sub><sup>+</sup>, SO<sub>4</sub><sup>2-</sup>, NO<sub>3</sub><sup>-</sup>, OC and EC), which is not achieved in previous studies. The background error covariance was calculated  
664 by ensemble perturbation based on adaptive uncertainties and non-Gaussian-distribution assumption of emission species. The  
665 DA experiments were conducted based on 33 observational sites in Northern China and surrounding areas.

666

667 NAQPMS-PDAF v2.0 with LKNETF can maintain high accuracy and reliability in ensemble DA with an ensemble size of 10,  
668 smaller than the traditional minimum of 20 ensemble members, as observed in prior ensemble assimilation studies. The FR  
669 (free-run fields without DA) have a poor consistency with the observations, with the CORR values ranging from 0.32-0.56  
670 and the R<sup>2</sup> values less than 0.3, showing that SO<sub>4</sub><sup>2-</sup>, OC and EC are significantly overestimated, while NH<sub>4</sub><sup>+</sup> and NO<sub>3</sub><sup>-</sup> are  
671 underestimated. A significant improvement was observed in the ANA (analysis fields) of the DA sites. The CORR values are  
672 not less than 0.86, the RMSE and MAE values do not exceed 3.23 μg/m<sup>3</sup> and 1.49 μg/m<sup>3</sup>, respectively, and R<sup>2</sup> is not less than  
673 0.74. Specifically, the CORR values for NO<sub>3</sub><sup>-</sup>, OC, and EC are not less than 0.96, and R<sup>2</sup> is not less than 0.93. The error  
674 distributions of the five chemical components concentrate to 0 with the mean bias ranging from 0±0.08 μg/m<sup>3</sup> to 1.02±3.07  
675 μg/m<sup>3</sup>. These improvements are also found in the ANA at VE sites, indicating an excellent DA performance of NAQPMS-



676 PDAF v2.0.

677

678 The ability of NAQPMS-PDAF v2.0 to interpret the spatiotemporal characteristics of the five chemical components was  
679 examined. For temporal variations, compared to the FR and FOR (forecast fields), the ANA closely aligned with the OBS  
680 (observations) and accurately captured the peak concentrations of  $\text{SO}_4^{2-}$ ,  $\text{NO}_3^-$ , and  $\text{NH}_4^+$  on specific periods (such as February  
681 25<sup>th</sup>), indicating good consistency and accurate characterization. Specifically, the CORR of the ANA at the six representative  
682 sites increased by 13.64%-89.58% and 17.19%-75.00%, respectively, while the RMSE decreased by 56.03%-83.13% and  
683 40.74%-72.20%. For spatial distributions, after DA, both  $\text{NH}_4^+$  and  $\text{NO}_3^-$  with positive analysis increments exhibit significant  
684 improvements in CORR and RMSE, as most DA sites show improvements of over 150% in CORR and over 50% in RMSE.  
685  $\text{SO}_4^{2-}$ , OC, and EC with negative analysis increments were also improved. Especially for OC and EC, the improvements of  
686 CORR and RMSE at most DA sites were over 200% and over 90%, respectively. The improvements at VE sites were also  
687 identified. Consequently, DA successfully aligned the spatiotemporal characteristics of the ANA with OBS and significantly  
688 reduced the biases of five chemical components.

689

690 Compared to the global reanalysis datasets (CORR: 0.42-0.55, RMSE: 4.51-12.27  $\mu\text{g}/\text{m}^3$ ) and NAQPMS-PDAF v1.0 (CORR:  
691 0.35-0.98, RMSE: 2.46-15.50  $\mu\text{g}/\text{m}^3$ ), the NAQPMS-PDAF v2.0 (CORR: 0.86-0.99, RMSE: 0.14-3.18  $\mu\text{g}/\text{m}^3$ ) has significant  
692 superiority in generating the reanalysis datasets of the  $\text{PM}_{2.5}$  chemical compositions with high spatiotemporal resolution.  
693 Besides, NAQPMS-PDAF v1.0 cannot capture the high-value concentrations and exhibits poor performance when interpreting  
694  $\text{SO}_4^{2-}$ , OC, and EC with CORR values ranging from 0.35 to 0.57. In contrast, NAQPMS-PDAF v2.0 interprets the five chemical  
695 components more accurately and consistently.

696

697 Finally, the uncertainties of NAQPMS-PDAF v2.0 are examined by identifying the influence of ensemble generation on  
698 ensemble DA performance. The non-Gaussian-distribution assumption outperforms the Gaussian-distribution assumption in  
699 NAQPMS-PDAF v2.0. Positive skewness performs better than negative skewness, and excessively high kurtosis should be  
700 avoided. Additionally, appropriately increasing the uncertainty of  $\text{SO}_2$  enhances the DA performance of  $\text{NH}_4^+$  and  $\text{SO}_4^{2-}$ . Future  
701 studies should conduct more sensitivity experiments on emission species perturbation to determine the suitable schemes for  
702 different aerosol chemical components.

703

704 The novel hybrid nonlinear DA system (NAQPMS-PDAF v2.0) can be effectively applied in the interpretation of chemical  
705 components and outperform in generating the reanalysis dataset of the five  $\text{PM}_{2.5}$  chemical components with high accuracy  
706 and high consistency, thus providing the sufficient channel to investigate the spatiotemporal characteristics, identify the  
707 regional transport and prevent and control aerosol composition pollution. In future work, we plan to research the vertical DA



708 of chemical components, introduce more vertical information from more observational platforms, and verify the simultaneous  
709 DA performance of surface and vertical mass concentrations.

710

#### 711 **Code and data availability**

712 The source codes in our work are available online via Zenodo (<https://doi.org/10.5281/zenodo.10886914>).

#### 713 **Author contributions**

714 HL developed the data assimilation system, performed numerical experiments, carried out the analysis and wrote the original  
715 manuscript. TY provided scientific guidance, designed the paper structure and wrote this paper. LN developed PDAF and  
716 provided help for the model code. DWZ, DZ, and GT provided PM<sub>2.5</sub> chemical component data. HW provided help for the  
717 model code. YS, PF, HS, ZW did overall supervision. All authors reviewed and revised this paper.

#### 718 **Competing interests**

719 The contact author has declared that neither they nor their co-authors have any competing interests.

#### 720 **Acknowledgements**

721 This work was supported by the National Key Research and Development Program for Young Scientists of China (No.  
722 2022YFC3704000), the National Natural Science Foundation of China (No. 42275122) and the National Key Scientific and  
723 Technological Infrastructure project “Earth System Science Numerical Simulator Facility” (EarthLab). Ting Yang would like  
724 to express gratitude towards the Program of the Youth Innovation Promotion Association (CAS). We thank the Big Data Cloud  
725 Service Infrastructure Platform (BDCSIP) for providing computing resources.

726



## 727 Reference

- 728 Aleksankina, K., Heal, M. R., Dore, A. J., Van Oijen, M., and Reis, S.: Global sensitivity and uncertainty analysis of an  
729 atmospheric chemistry transport model: the FRAME model (version 9.15.0) as a case study, *Geosci. Model Dev.*, 11, 1653-  
730 1664, <https://doi.org/10.5194/gmd-11-1653-2018>, 2018.
- 731 Ali, A., Amin, S. E., Ramadan, H. H., and Tolba, M. F.: Enhancement of OMI aerosol optical depth data assimilation using  
732 artificial neural network, *Neural Computing and Applications*, 23, 2267-2279, <https://doi.org/10.1007/s00521-012-1178-9>,  
733 2013.
- 734 Alves, C., Evtyugina, M., Vicente, E., Vicente, A., Rienda, I. C., de la Campa, A. S., Tomé, M., and Duarte, I.: PM<sub>2.5</sub> chemical  
735 composition and health risks by inhalation near a chemical complex, *J. Environ. Sci.*, 124, 860-874,  
736 <https://doi.org/10.1016/j.jes.2022.02.013>, 2023.
- 737 Amante, C. and Eakins, B. W.: ETOPO1 arc-minute global relief model: procedures, data sources and analysis, 2009.
- 738 Arthur, D. and Vassilvitskii, S.: K-means++: the advantages of careful seeding, *Proceedings of the eighteenth annual ACM-  
739 SIAM symposium on Discrete algorithms*, 1027-1035, <https://dl.acm.org/doi/10.5555/1283383.1283494>, 2007
- 740 Bao, Y., Zhu, L., Guan, Q., Guan, Y., Lu, Q., Petropoulos, G. P., Che, H., Ali, G., Dong, Y., Tang, Z., Gu, Y., Tang, W., and  
741 Hou, Y.: Assessing the impact of Chinese FY-3/MERSI AOD data assimilation on air quality forecasts: Sand dust events in  
742 northeast China, *Atmos. Environ.*, 205, 78-89, <https://doi.org/10.1016/j.atmosenv.2019.02.026>, 2019.
- 743 Bell, M. L., Dominici, F., Ebisu, K., Zeger, S. L., and Samet, J. M.: Spatial and temporal variation in PM<sub>2.5</sub> chemical  
744 composition in the United States for health effects studies, *Environ. Health Perspect.*, 115, 989-995,  
745 <https://doi.org/10.1289/ehp.9621>, 2007.
- 746 Bishop, C. H., Etherton, B. J., and Majumdar, S. J.: Adaptive Sampling with the Ensemble Transform Kalman Filter. Part I:  
747 Theoretical Aspects, *Mon. Weather Rev.*, 129, 420-436, [https://doi.org/10.1175/1520-  
0493\(2001\)129<0420:ASWTET>2.0.CO;2](https://doi.org/10.1175/1520-<br/>748 0493(2001)129<0420:ASWTET>2.0.CO;2), 2001.
- 749 Cao, J. J., Lee, S. C., Chow, J. C., Watson, J. G., Ho, K. F., Zhang, R. J., Jin, Z. D., Shen, Z. X., Chen, G. C., Kang, Y. M., Zou,  
750 S. C., Zhang, L. Z., Qi, S. H., Dai, M. H., Cheng, Y., and Hu, K.: Spatial and seasonal distributions of carbonaceous aerosols  
751 over China, *J. Geophys Res.-Atmos.*, 112, <https://doi.org/10.1029/2006jd008205>, 2007.
- 752 Chai, T., Kim, H. C., Pan, L., Lee, P., and Tong, D.: Impact of moderate resolution imaging spectroradiometer aerosol optical  
753 depth and airnow PM<sub>2.5</sub> assimilation on community multi-scale air quality aerosol predictions over the contiguous United  
754 States, *J. Geophys Res.*, 122, 5399-5415, <https://doi.org/10.1002/2016JD026295>, 2017.
- 755 Chang, W., Zhang, Y., Li, Z., Chen, J., and Li, K.: Improving the sectional Model for Simulating Aerosol Interactions and  
756 Chemistry (MOSAIC) aerosols of the Weather Research and Forecasting-Chemistry (WRF-Chem) model with the revised  
757 Gridpoint Statistical Interpolation system and multi-wavelength aerosol optical measurements: The dust aerosol observation  
758 campaign at Kashi, near the Taklimakan Desert, northwestern China, *Atmos. Chem. Phys.*, 21, 4403-4430,  
759 <https://doi.org/10.5194/acp-21-4403-2021>, 2021.
- 760 Chang, W., Liao, H., Xin, J., Li, Z., Li, D., and Zhang, X.: Uncertainties in anthropogenic aerosol concentrations and direct  
761 radiative forcing induced by emission inventories in eastern China, *Atmos. Res.*, 166, 129-140,  
762 <https://doi.org/10.1016/j.atmosres.2015.06.021>, 2015.
- 763 Cheng, Y., Dai, T., Goto, D., A J Schutgens, N., Shi, G., and Nakajima, T.: Investigating the assimilation of CALIPSO global  
764 aerosol vertical observations using a four-dimensional ensemble Kalman filter, *Atmos. Chem. Phys.*, 19, 13445-13467,  
765 <https://doi.org/10.5194/acp-19-13445-2019>, 2019.
- 766 Constantinescu, E. M., Sandu, A., Chai, T., and Carmichael, G. R.: Assessment of ensemble-based chemical data assimilation  
767 in an idealized setting, *Atmos. Environ.*, 41, 18-36, <https://doi.org/10.1016/j.atmosenv.2006.08.006>, 2007.
- 768 Dai, T., Schutgens, N. A. J., Goto, D., Shi, G., and Nakajima, T.: Improvement of aerosol optical properties modeling over  
769 Eastern Asia with MODIS AOD assimilation in a global non-hydrostatic icosahedral aerosol transport model, *Environ. Pollut.*,  
770 195, 319-329, <https://doi.org/10.1016/j.envpol.2014.06.021>, 2014.
- 771 Du, W., Dada, L., Zhao, J., Chen, X., Daellenbach, K. R., Xie, C., Wang, W., He, Y., Cai, J., Yao, L., Zhang, Y., Wang, Q., Xu,  
772 W., Wang, Y., Tang, G., Cheng, X., Kokkonen, T. V., Zhou, W., Yan, C., Chu, B., Zha, Q., Hakala, S., Kurppa, M., Järvi, L.,  
773 Liu, Y., Li, Z., Ge, M., Fu, P., Nie, W., Bianchi, F., Petäjä, T., Paasonen, P., Wang, Z., Worsnop, D. R., Kerminen, V.-M.,



- 774 Kulmala, M., and Sun, Y.: A 3D study on the amplification of regional haze and particle growth by local emissions, *npj Climate*  
775 *and Atmospheric Science*, 4, 4, <https://doi.org/10.1038/s41612-020-00156-5>, 2021.
- 776 Evensen, G.: Sequential data assimilation with a nonlinear quasi-geostrophic model using Monte Carlo methods to forecast  
777 error statistics, *J. Geophys. Res.*, 99, <https://doi.org/10.1029/94jc00572>, 1994.
- 778 Evensen, G.: The Ensemble Kalman Filter: Theoretical formulation and practical implementation, *Ocean Dynamics*, 53, 343-  
779 367, <https://doi.org/10.1007/s10236-003-0036-9>, 2003.
- 780 Friedman, J. H., Bentley, J. L., and Finkel, R. A.: An algorithm for finding best matches in logarithmic expected time, *ACM T.*  
781 *Math. Software*, 3, 209-226, <https://doi.org/10.1145/355744.355745>, 1977.
- 782 Ge, B., Wang, Z., Xu, X., Wu, J., Yu, X., and Li, J.: Wet deposition of acidifying substances in different regions of China and  
783 the rest of East Asia: Modeling with updated NAQPMS, *Environ. Pollut.*, 187, 10-21,  
784 <https://doi.org/10.1016/j.envpol.2013.12.014>, 2014.
- 785 Ge, X., He, Y., Sun, Y., Xu, J., Wang, J., Shen, Y., and Chen, M.: Characteristics and Formation Mechanisms of Fine Particulate  
786 Nitrate in Typical Urban Areas in China, *Atmosphere*, 8, <https://doi.org/10.3390/atmos8030062>, 2017.
- 787 Gordon, N. J., Salmund, D. J., and Smith, A. F.: Novel approach to nonlinear/non-Gaussian Bayesian state estimation, *IEE*  
788 *Proc.-F*, 140, 107-113, <https://doi.org/10.1049/ip-f-2.1993.0015>, 1993.
- 789 Guo, Y.: Characteristics of size-segregated carbonaceous aerosols in the Beijing-Tianjin-Hebei region, *Environ. Sci. Pollut. R.*,  
790 23, 13918-13930, <https://doi.org/10.1007/s11356-016-6538-z>, 2016.
- 791 Ha, S.: Implementation of aerosol data assimilation in WRFDA (v4.0.3) for WRF-Chem (v3.9.1) using the RACM/MADE-  
792 VBS scheme, *Geosci. Model Dev.*, 15, 1769-1788, <https://doi.org/10.5194/gmd-15-1769-2022>, 2022.
- 793 Hamill, T. M. and Snyder, C.: A Hybrid Ensemble Kalman Filter–3D Variational Analysis Scheme, *Mon. Weather Rev.*, 128,  
794 2905-2919, [https://doi.org/10.1175/1520-0493\(2000\)128<2905:AHEKFV>2.0.CO;2](https://doi.org/10.1175/1520-0493(2000)128<2905:AHEKFV>2.0.CO;2), 2000.
- 795 Hersbach, H.: Decomposition of the continuous ranked probability score for ensemble prediction systems, *Wea. Forecasting*,  
796 15, 559-570, [https://doi.org/10.1175/1520-0434\(2000\)015<0559:DOTCRP>2.0.CO;2](https://doi.org/10.1175/1520-0434(2000)015<0559:DOTCRP>2.0.CO;2), 2000.
- 797 Horowitz, L. W., Walters, S., Mauzerall, D. L., Emmons, L. K., Rasch, P. J., Granier, C., Tie, X., Lamarque, J. F., Schultz, M.  
798 G., Tyndall, G. S., Orlando, J. J., and Brasseur, G.P.: A global simulation of tropospheric ozone and related tracers: Description  
799 and evaluation of MOZART, version 2, *J. Geophys. Res.-Atmos.*, 108, <https://doi.org/10.1029/2002JD002853>, 2003.
- 800 Houtekamer, P. L. and Zhang, F.: Review of the Ensemble Kalman Filter for Atmospheric Data Assimilation, *Mon. Weather*  
801 *Rev.*, 144, 4489-4532, <https://doi.org/10.1175/mwr-d-15-0440.1>, 2016.
- 802 Huang, B., Pagowski, M., Trahan, S., Martin, C. R., Tangborn, A., Kondragunta, S., and Kleist, D. T.: JEDI-Based Three-  
803 Dimensional Ensemble-Variational Data Assimilation System for Global Aerosol Forecasting at NCEP, *J. Adv. Model. Earth*  
804 *Sy.*, 15, <https://doi.org/10.1029/2022ms003232>, 2023.
- 805 Huang, Y., Wu, S., Dubey, M. K., and French, N. H. F.: Impact of aging mechanism on model simulated carbonaceous aerosols,  
806 *Atmos. Chem. Phys.*, 13, 6329-6343, <https://doi.org/10.5194/acp-13-6329-2013>, 2013.
- 807 Huneus, N., Boucher, O., and Chevallier, F.: Atmospheric inversion of SO<sub>2</sub> and primary aerosol emissions for the year 2010,  
808 *Atmos. Chem. Phys.*, 13, 6555-6573, <https://doi.org/10.5194/acp-13-6555-2013>, 2013.
- 809 Huneus, N., Chevallier, F., and Boucher, O.: Estimating aerosol emissions by assimilating observed aerosol optical depth in  
810 a global aerosol model, *Atmos. Chem. Phys.*, 12, 4585-4606, <https://doi.org/10.5194/acp-12-4585-2012>, 2012.
- 811 Hunt, B. R., Kostelich, E. J., and Szunyogh, I.: Efficient data assimilation for spatiotemporal chaos: A local ensemble transform  
812 Kalman filter, *Physica D*, 230, 112-126, <https://doi.org/10.1016/j.physd.2006.11.008>, 2007.
- 813 Inness, A., Ades, M., Agustí-Panareda, A., Barré, J., Benedictow, A., Blechschmidt, A. M., Dominguez, J. J., Engelen, R.,  
814 Eskes, H., Flemming, J., Huijnen, V., Jones, L., Kipling, Z., Massart, S., Parrington, M., Peuch, V. H., Razinger, M., Remy, S.,  
815 Schulz, M., and Suttie, M.: The CAMS reanalysis of atmospheric composition, *Atmos. Chem. Phys.*, 19, 3515-3556,  
816 <https://doi.org/10.5194/acp-19-3515-2019>, 2019.
- 817 Jia, J., Cheng, S., Liu, L., Lang, J., Wang, G., Chen, G., and Liu, X.: An Integrated WRF-CAMx Modeling Approach for  
818 Impact Analysis of Implementing the Emergency PM<sub>2.5</sub> Control Measures during Red Alerts in Beijing in December 2015,  
819 *Aerosol Air Qual. Res.*, 17, 2491-2508, <https://doi.org/10.4209/aaqr.2017.01.0009>, 2017.
- 820 Jin, J., Segers, A., Heemink, A., Yoshida, M., Han, W., and Lin, H. X.: Dust Emission Inversion Using Himawari-8 AODs





- 821 Over East Asia: An Extreme Dust Event in May 2017, *J. Adv. Model. Earth Sy.*, 11, 446-467,  
822 <https://doi.org/10.1029/2018MS001491>, 2019.
- 823 Jolliffe, I. T. and Stephenson, D. B.: Forecast verification: a practitioner's guide in atmospheric science, John Wiley & Sons,  
824 <https://doi.org/10.1002/9781119960003>, 2012.
- 825 Khanna, I., Khare, M., Gargava, P., and Khan, A. A.: Effect of PM<sub>2.5</sub> chemical constituents on atmospheric visibility impairment,  
826 *Journal of the Air & Waste Management Association*, 68, 430-437, <https://doi.org/10.1080/10962247.2018.1425772>, 2018.
- 827 Kim, G., Lee, S., Im, J., Song, C.-K., Kim, J., and Lee, M.-i.: Aerosol data assimilation and forecast using Geostationary Ocean  
828 Color Imager aerosol optical depth and in-situ observations during the KORUS-AQ observing period, *GISci. Remote Sens.*,  
829 58, 1175-1194, <https://doi.org/10.1080/15481603.2021.1972714>, 2021.
- 830 Kong, L., Tang, X., Zhu, J., Wang, Z., Li, J., Wu, H., Wu, Q., Chen, H., Zhu, L., Wang, W., Liu, B., Wang, Q., Chen, D., Pan,  
831 Y., Song, T., Li, F., Zheng, H., Jia, G., Lu, M., Wu, L., and Carmichael, G. R.: A 6-year-long (2013–2018) high-resolution air  
832 quality reanalysis dataset in China based on the assimilation of surface observations from CNEMC, *Earth Syst. Sci. Data*, 13,  
833 529-570, <https://doi.org/10.5194/essd-13-529-2021>, 2021.
- 834 Kumar, R., Ghude, S. D., Biswas, M., Jena, C., Alessandrini, S., Debnath, S., Kulkarni, S., Sperati, S., Soni, V. K., Nanjundiah,  
835 R. S., and Rajeevan, M.: Enhancing Accuracy of Air Quality and Temperature Forecasts During Paddy Crop Residue Burning  
836 Season in Delhi Via Chemical Data Assimilation, *J. Geophys Res.-Atmos.*, 125, <https://doi.org/10.1029/2020JD033019>, 2020.
- 837 Kurtz, W., He, G., Kollet, S. J., Maxwell, R. M., Vereecken, H., and Hendricks Franssen, H. J.: TerrSysMP-PDAF (version  
838 1.0): a modular high-performance data assimilation framework for an integrated land surface–subsurface model, *Geosci.*  
839 *Model Dev.*, 9, 1341-1360, <https://doi.org/10.5194/gmd-9-1341-2016>, 2016.
- 840 Lawson, W. G. and Hansen, J. A.: Implications of Stochastic and Deterministic Filters as Ensemble-Based Data Assimilation  
841 Methods in Varying Regimes of Error Growth, *Mon. Weather Rev.*, 132, 1966-1981, [https://doi.org/10.1175/1520-0493\(2004\)132<1966:IOSADF>2.0.CO;2](https://doi.org/10.1175/1520-0493(2004)132<1966:IOSADF>2.0.CO;2), 2004.
- 842 Li, J., Li, X., Carlson, B. E., Kahn, R. A., Laci, A. A., Dubovik, O., and Nakajima, T.: Reducing multisensor satellite monthly  
843 mean aerosol optical depth uncertainty: 1. Objective assessment of current AERONET locations, *J. Geophys Res.-Atmos.*, 121,  
844 609-627, <https://doi.org/10.1002/2016JD025469>, 2016.
- 845 Li, J., Dong, Y., Song, Y., Dong, B., van Donkelaar, A., Martin, R. V., Shi, L., Ma, Y., Zou, Z., and Ma, J.: Long-term effects  
846 of PM<sub>2.5</sub> components on blood pressure and hypertension in Chinese children and adolescents, *Environ. Int.*, 161, 107134,  
847 <https://doi.org/10.1016/j.envint.2022.107134>, 2022a.
- 848 Li, S., Chen, L., Huang, G., Lin, J., Yan, Y., Ni, R., Huo, Y., Wang, J., Liu, M., Weng, H., Wang, Y., and Wang, Z.: Retrieval  
849 of surface PM<sub>2.5</sub> mass concentrations over North China using visibility measurements and GEOS-Chem simulations, *Atmos.*  
850 *Environ.*, 222, <https://doi.org/10.1016/j.atmosenv.2019.117121>, 2020.
- 851 Li, Y., Wang, X., Li, J., Zhu, L., and Chen, Y.: Numerical Simulation of Topography Impact on Transport and Source  
852 Apportionment on PM<sub>2.5</sub> in a Polluted City in Fenwei Plain, *Atmosphere*, 13, 233, <https://doi.org/10.3390/atmos13020233>,  
853 2022b.
- 854 Lin, G. Y., Chen, H. W., Chen, B. J., and Chen, S. C.: A machine learning model for predicting PM<sub>2.5</sub> and nitrate concentrations  
855 based on long-term water-soluble inorganic salts datasets at a road site station, *Chemosphere*, 289,  
856 <https://doi.org/10.1016/j.chemosphere.2021.133123>, 2022.
- 857 Liu, Y., Liu, J., Li, C., Yu, F., and Wang, W.: Effect of the Assimilation Frequency of Radar Reflectivity on Rain Storm  
858 Prediction by Using WRF-3DVAR, *Remote Sens.*, 13, <https://doi.org/10.3390/rs13112103>, 2021.
- 859 Lloyd, S.: Least squares quantization in PCM, *IEEE T. Inform. Theory*, 28, 129-137, <https://doi.org/10.1109/TIT.1982.1056489>,  
860 1982.
- 861 Luo, X., Liu, X., Pan, Y., Wen, Z., Xu, W., Zhang, L., Kou, C., Lv, J., and Goulding, K.: Atmospheric reactive nitrogen  
862 concentration and deposition trends from 2011 to 2018 at an urban site in north China, *Atmos. Environ.*, 224,  
863 <https://doi.org/10.1016/j.atmosenv.2020.117298>, 2020.
- 864 Lv, Z., Wei, W., Cheng, S., Han, X., and Wang, X.: Meteorological characteristics within boundary layer and its influence on  
865 PM<sub>2.5</sub> pollution in six cities of North China based on WRF-Chem, *Atmos. Environ.*, 228,  
866 <https://doi.org/10.1016/j.atmosenv.2020.117417>, 2020.
- 867



- 868 Lynch, P., Reid, J. S., Westphal, D. L., Zhang, J., Hogan, T. F., Hyer, E. J., Curtis, C. A., Hegg, D. A., Shi, Y., Campbell, J. R.,  
869 Rubin, J. I., Sessions, W. R., Turk, F. J., and Walker, A. L.: An 11-year global gridded aerosol optical thickness reanalysis (v1.0)  
870 for atmospheric and climate sciences, *Geosci. Model Dev.*, 9, 1489-1522, <https://doi.org/10.5194/gmd-9-1489-2016>, 2016.
- 871 Mallet, V. and Sportisse, B.: Uncertainty in a chemistry-transport model due to physical parameterizations and numerical  
872 approximations: An ensemble approach applied to ozone modeling, *J. Geophys. Res.-Atmos.*, 111,  
873 <https://doi.org/10.1029/2005jd006149>, 2006.
- 874 Miao, R., Chen, Q., Zheng, Y., Cheng, X., Sun, Y., Palmer, P. I., Shrivastava, M., Guo, J., Zhang, Q., Liu, Y., Tan, Z., Ma, X.,  
875 Chen, S., Zeng, L., Lu, K., and Zhang, Y.: Model bias in simulating major chemical components of PM<sub>2.5</sub> in China, *Atmos.*  
876 *Chem. Phys.*, 20, 12265-12284, <https://doi.org/10.5194/acp-20-12265-2020>, 2020.
- 877 Ming, L., Jin, L., Li, J., Fu, P., Yang, W., Liu, D., Zhang, G., Wang, Z., and Li, X. J. E. p.: PM<sub>2.5</sub> in the Yangtze River Delta,  
878 China: Chemical compositions, seasonal variations, and regional pollution events, 223, 200-212, 2017.
- 879 Mingari, L., Folch, A., Prata, A. T., Pardini, F., Macedonio, G., and Costa, A.: Data assimilation of volcanic aerosol  
880 observations using FALL3D+PDAF, *Atmos. Chem. Phys.*, 22, 1773-1792, <https://doi.org/10.5194/acp-22-1773-2022>, 2022.
- 881 Miyazaki, K., Eskes, H. J., Sudo, K., Takigawa, M., van Weele, M., and Boersma, K. F.: Simultaneous assimilation of satellite  
882 NO<sub>2</sub>, O<sub>3</sub>, CO, and HNO<sub>3</sub> data for the analysis of tropospheric chemical composition and emissions, *Atmos. Chem. Phys.*, 12,  
883 9545-9579, <https://doi.org/10.5194/acp-12-9545-2012>, 2012.
- 884 Nerger, L.: On Serial Observation Processing in Localized Ensemble Kalman Filters, *Mon. Weather Rev.*, 143, 1554-1567,  
885 <https://doi.org/10.1175/mwr-d-14-00182.1>, 2015.
- 886 Nerger, L.: Data assimilation for nonlinear systems with a hybrid nonlinear Kalman ensemble transform filter, *Q. J. Roy.*  
887 *Meteor. Soc.*, 148, 620-640, <https://doi.org/10.1002/qj.4221>, 2022.
- 888 Nerger, L., Tang, Q., and Mu, L.: Efficient ensemble data assimilation for coupled models with the Parallel Data Assimilation  
889 Framework: example of AWI-CM (AWI-CM-PDAF 1.0), *Geosci. Model Dev.*, 13, 4305-4321, <https://doi.org/10.5194/gmd-13-4305-2020>, 2020.
- 891 Nerger, L., Janjić, T., Schröter, J., and Hiller, W.: A Unification of Ensemble Square Root Kalman Filters, *Mon. Weather Rev.*,  
892 140, 2335-2345, <https://doi.org/10.1175/mwr-d-11-00102.1>, 2012.
- 893 Nishizawa, T., Sugimoto, N., Matsui, I., Shimizu, A., and Okamoto, H.: Algorithms to retrieve optical properties of three  
894 component aerosols from two-wavelength backscatter and one-wavelength polarization lidar measurements considering  
895 nonsphericity of dust, *J. Quant. Spectrosc. Ra.*, 112, 254-267, <https://doi.org/10.1016/j.jqsrt.2010.06.002>, 2011.
- 896 Nishizawa, T., Okamoto, H., Takemura, T., Sugimoto, N., Matsui, I., and Shimizu, A.: Aerosol retrieval from two-wavelength  
897 backscatter and one-wavelength polarization lidar measurement taken during the MR01K02 cruise of the R/V Mirai and  
898 evaluation of a global aerosol transport model, *J. Geophys. Res.-Atmos.*, 113, <https://doi.org/10.1029/2007jd009640>, 2008.
- 899 Nishizawa, T., Sugimoto, N., Matsui, I., Shimizu, A., Hara, Y., Itsushi, U., Yasunaga, K., Kudo, R., and Kim, S. W.: Ground-  
900 based network observation using Mie-Raman lidars and multi-wavelength Raman lidars and algorithm to retrieve distributions  
901 of aerosol components, *J. Quant. Spectrosc. Ra.*, 188, 79-93, <https://doi.org/10.1016/j.jqsrt.2016.06.031>, 2017.
- 902 Park, R. S., Lee, S., Shin, S. K., and Song, C. H.: Contribution of ammonium nitrate to aerosol optical depth and direct radiative  
903 forcing by aerosols over East Asia, *Atmos. Chem. Phys.*, 14, 2185-2201, <https://doi.org/10.5194/acp-14-2185-2014>, 2014.
- 904 Randles, C. A., da Silva, A. M., Buchard, V., Colarco, P. R., Darmenov, A., Govindaraju, R., Smirnov, A., Holben, B., Ferrare,  
905 R., Hair, J., Shinozuka, Y., and Flynn, C. J.: The MERRA-2 aerosol reanalysis, 1980 onward. Part I: System description and  
906 data assimilation evaluation, *J. Climate*, 30, 6823-6850, <https://doi.org/10.1175/JCLI-D-16-0609.1>, 2017.
- 907 Rodriguez, M. A., Brouwer, J., Samuelsen, G. S., and Dabdub, D.: Air quality impacts of distributed power generation in the  
908 South Coast Air Basin of California 2: Model uncertainty and sensitivity analysis, *Atmos. Environ.*, 41, 5618-5635,  
909 <https://doi.org/10.1016/j.atmosenv.2007.02.049>, 2007.
- 910 Rubin, J. I. and Collins, W. D.: Global simulations of aerosol amount and size using MODIS observations assimilated with an  
911 Ensemble Kalman Filter, *J. Geophys. Res. Atmospheres*, 119, 12,780-712,806, <https://doi.org/10.1002/2014JD021627>, 2014.
- 912 Rubin, J. I., Reid, J. S., Hansen, J. A., Anderson, J. L., Holben, B. N., Xian, P., Westphal, D. L., and Zhang, J. L.: Assimilation  
913 of AERONET and MODIS AOT observations using variational and ensemble data assimilation methods and its impact on  
914 aerosol forecasting skill, *J. Geophys. Res.-Atmospheres*, 122, 4967-4992, <https://doi.org/10.1002/2016jd026067>, 2017.



- 915 Saide, P. E., Kim, J., Song, C. H., Choi, M., Cheng, Y., and Carmichael, G. R.: Assimilation of next generation geostationary  
916 aerosol optical depth retrievals to improve air quality simulations, *Geophys. Res. Lett.*, 41, 9188-9196,  
917 <https://doi.org/10.1002/2014GL062089>, 2014.
- 918 Sax, T. and Isakov, V.: A case study for assessing uncertainty in local-scale regulatory air quality modeling applications, *Atmos.*  
919 *Environ.*, 37, 3481-3489, [https://doi.org/10.1016/S1352-2310\(03\)00411-4](https://doi.org/10.1016/S1352-2310(03)00411-4), 2003.
- 920 Schlesinger, R. B.: The health impact of common inorganic components of fine particulate matter (PM<sub>2.5</sub>) in ambient air: a  
921 critical review, *Inhal. Toxicol.*, 19, 811-832, <https://doi.org/10.1080/08958370701402382>, 2007.
- 922 Schult, I., Feichter, J., and Cooke, W. F.: Effect of black carbon and sulfate aerosols on the Global Radiation Budget, *J. Geophys*  
923 *Res.-Atmospheres*, 102, 30107-30117, <https://doi.org/10.1029/97jd01863>, 1997.
- 924 Schutgens, N. A. J., Miyoshi, T., Takemura, T., and Nakajima, T.: Applying an ensemble Kalman filter to the assimilation of  
925 AERONET observations in a global aerosol transport model, *Atmos. Chem. Phys.*, 10, 2561-2576, <https://doi.org/10.5194/acp-10-2561-2010>, 2010.
- 927 Schwartz, C. S., Liu, Z., Lin, H.-C., and Cetola, J. D.: Assimilating aerosol observations with a "hybrid" variational-ensemble  
928 data assimilation system, *J. Geophys Res.-Atmospheres*, 119, 4043-4069, <https://doi.org/10.1002/2013jd020937>, 2014.
- 929 Soni, A., Mandariya, A. K., Rajeev, P., Izhar, S., Singh, G. K., Choudhary, V., Qadri, A. M., Gupta, A. D., Singh, A. K., and  
930 Gupta, T.: Multiple site ground-based evaluation of carbonaceous aerosol mass concentrations retrieved from CAMS and  
931 MERRA-2 over the Indo-Gangetic Plain, *Environm. Sci.-Atmos.*, 1, 577-590, <https://doi.org/10.1039/d1ea00067e>, 2021.
- 932 Strebel, L., Bogena, H. R., Vereecken, H., and Hendricks Franssen, H. J.: Coupling the Community Land Model version 5.0  
933 to the parallel data assimilation framework PDAF: description and applications, *Geosci. Model Dev.*, 15, 395-411,  
934 <https://doi.org/10.5194/gmd-15-395-2022>, 2022.
- 935 Su Lee, Y., Choi, E., Park, M., Jo, H., Park, M., Nam, E., Gon Kim, D., Yi, S.-M., and Young Kim, J.: Feature Extraction and  
936 Prediction of Fine Particulate Matter (PM<sub>2.5</sub>) Chemical Constituents using Four Machine Learning Models, *Expert Syst. Appl.*,  
937 119696, <https://doi.org/10.1016/j.eswa.2023.119696>, 2023.
- 938 Talagrand, O. and Courtier, P.: Variational Assimilation of Meteorological Observations With the Adjoint Vorticity Equation.  
939 I: Theory, *Q. J. Roy. Meteor. Soc.*, 113, 1311-1328, <https://doi.org/10.1002/qj.49711347812>, 1987.
- 940 Tang, Y., Chai, T., Pan, L., Lee, P., Tong, D., Kim, H. C., and Chen, W.: Using optimal interpolation to assimilate surface  
941 measurements and satellite AOD for ozone and PM<sub>2.5</sub>: A case study for July 2011, *Journal of the Air and Waste Management*  
942 *Association*, 65, 1206-1216, <https://doi.org/10.1080/10962247.2015.1062439>, 2015.
- 943 Tippett, M. K., Anderson, J. L., Bishop, C. H., Hamill, T. M., and Whitaker, J. S.: Ensemble Square Root Filters, *Mon. Weather*  
944 *Rev.*, 131, 1485-1490, [https://doi.org/10.1175/1520-0493\(2003\)131<1485:ESRF>2.0.CO;2](https://doi.org/10.1175/1520-0493(2003)131<1485:ESRF>2.0.CO;2), 2003.
- 945 Tödter, J. and Ahrens, B.: A Second-Order Exact Ensemble Square Root Filter for Nonlinear Data Assimilation, *Mon. Weather*  
946 *Rev.*, 143, 1347-1367, <https://doi.org/10.1175/MWR-D-14-00108.1>, 2015.
- 947 Tödter, J., Kirchgessner, P., Nerger, L., and Ahrens, B.: Assessment of a Nonlinear Ensemble Transform Filter for High-  
948 Dimensional Data Assimilation, *Mon. Weather Rev.*, 144, 409-427, <https://doi.org/10.1175/MWR-D-15-0073.1>, 2016.
- 949 Tsikerdekis, A., Schutgens, N. A. J., and Hasekamp, O. P.: Assimilating aerosol optical properties related to size and absorption  
950 from POLDER/PARASOL with an ensemble data assimilation system, *Atmos. Chem. Phys.*, 21, 2637-2674,  
951 <https://doi.org/10.5194/acp-21-2637-2021>, 2021.
- 952 Wang, H., Yang, T., Wang, Z., Li, J., Chai, W., Tang, G., Kong, L., and Chen, X.: An aerosol vertical data assimilation system  
953 (NAQPMS-PDAF v1.0): development and application, *Geosci. Model Dev.*, 15, 3555-3585, <https://doi.org/10.5194/gmd-15-3555-2022>, 2022.
- 954 Wang, N., H. Guo, Jiang, F., Ling, Z. H., and Wang, T.: Simulation of ozone formation at different elevations in mountainous  
955 area of Hong Kong using WRF-CMAQ model, *Sci. Total Environ.*, 505, 939-951,  
956 <https://doi.org/10.1016/j.scitotenv.2014.10.070>, 2015.
- 957 Wang, T., Liu, H., Li, J., Wang, S., Kim, Y., Sun, Y., Yang, W., Du, H., Wang, Z., and Wang, Z.: A two-way coupled regional  
958 urban-street network air quality model system for Beijing, China, *Geosci. Model Dev.*, 16, 5585-5599,  
959 <https://doi.org/10.5194/gmd-16-5585-2023>, 2023.
- 960 Wang, Z., Itahashi, S., Uno, I., Pan, X., Osada, K., Yamamoto, S., Nishizawa, T., Tamura, K., and Wang, Z.: Modeling the  
961



- 962 Long-Range Transport of Particulate Matters for January in East Asia using NAQPMS and CMAQ, *Aerosol Air Qual. Res.*,  
963 17, 3065-3078, <https://doi.org/10.4209/aaqr.2016.12.0534>, 2017.
- 964 Wang, Z., Uno, I., Yumimoto, K., Pan, X., Chen, X., Li, J., Wang, Z., Shimizu, A., and Sugimoto, N.: Dust Heterogeneous  
965 Reactions during Long-Range Transport of a Severe Dust Storm in May 2017 over East Asia, *Atmosphere*, 10, 680,  
966 <https://doi.org/10.3390/atmos10110680>, 2019.
- 967 Wang, Z., Li, J., Wang, Z., Yang, W., Tang, X., Ge, B., Yan, P., Zhu, L., Chen, X., Chen, H., Wand, W., Li, J., Liu, B., Wang,  
968 X., Wand, W., Zhao, Y., Lu, N., and Su, D.: Modeling study of regional severe hazes over mid-eastern China in January 2013  
969 and its implications on pollution prevention and control, *Sci. China Earth Sci.*, 57, 3-13, <https://doi.org/10.1007/s11430-013-4793-0>, 2014.
- 970  
971 Werner, M., Kryza, M., and Guzikowski, J.: Can Data Assimilation of Surface PM<sub>2.5</sub> and Satellite AOD Improve WRF-Chem  
972 Forecasting? A Case Study for Two Scenarios of Particulate Air Pollution Episodes in Poland, *Remote Sens.*, 11,  
973 <https://doi.org/10.3390/rs11202364>, 2019.
- 974 Wilcox, E. M., Thomas, R. M., Praveen, P. S., Pistone, K., Bender, F. A., and Ramanathan, V.: Black carbon solar absorption  
975 suppresses turbulence in the atmospheric boundary layer, *P. Natl. Acad. Sci. USA*, 113, 11794-11799,  
976 <https://doi.org/10.1073/pnas.1525746113>, 2016.
- 977 Xia, X., Min, J., Wang, Y., Shen, F., Yang, C., and Sun, Z.: Assimilating Himawari-8 AHI aerosol observations with a rapid-  
978 update data assimilation system, *Atmos. Environ.*, 215, <https://doi.org/10.1016/j.atmosenv.2019.116866>, 2019.
- 979 Xia, X., Min, J., Shen, F., Wang, Y., Xu, D., Yang, C., and Zhang, P.: Aerosol data assimilation using data from Fengyun-4A,  
980 a next-generation geostationary meteorological satellite, *Atmos. Environ.*, 237,  
981 <https://doi.org/10.1016/j.atmosenv.2020.117695>, 2020.
- 982 Xie, X., Hu, J., Qin, M., Guo, S., Hu, M., Wang, H., Lou, S., Li, J., Sun, J., Li, X., Sheng, L., Zhu, J., Chen, G., Yin, J., Fu, W.,  
983 Huang, C., and Zhang, Y.: Modeling particulate nitrate in China: Current findings and future directions, *Environ. Int.*, 166,  
984 107369, <https://doi.org/10.1016/j.envint.2022.107369>, 2022.
- 985 Yan, Y., Zhou, Y., Kong, S., Lin, J., Wu, J., Zheng, H., Zhang, Z., Song, A., Bai, Y., Ling, Z., Liu, D., and Zhao, T.: Effectiveness  
986 of emission control in reducing PM<sub>2.5</sub> pollution in central China during winter haze episodes under various potential synoptic  
987 controls, *Atmos. Chem. Phys.*, 21, 3143-3162, <https://doi.org/10.5194/acp-21-3143-2021>, 2021.
- 988 Yang, T., Li, H., Wang, H., Sun, Y., Chen, X., Wang, F., Xu, L., and Wang, Z.: Vertical aerosol data assimilation technology  
989 and application based on satellite and ground lidar: A review and outlook, *J. Environ. Sci.*, 123, 292-305,  
990 <https://doi.org/10.1016/j.jes.2022.04.012>, 2023.
- 991 Yang, X., Wu, Q., Zhao, R., Cheng, H., He, H., Ma, Q., Wang, L., and Luo, H.: New method for evaluating winter air quality:  
992 PM<sub>2.5</sub> assessment using Community Multi-Scale Air Quality Modeling (CMAQ) in Xi'an, *Atmos. Environ.*, 211, 18-28,  
993 <https://doi.org/10.1016/j.atmosenv.2019.04.019>, 2019.
- 994 Ye, Q., Li, J., Chen, X., Chen, H., Yang, W., Du, H., Pan, X., Tang, X., Wang, W., Zhu, L., Li, J., Wang, Z., and Wang, Z.:  
995 High-resolution modeling of the distribution of surface air pollutants and their intercontinental transport by a global  
996 tropospheric atmospheric chemistry source-receptor model (GNAQPMS-SM), *Geosci. Model Dev.*, 14, 7573-7604,  
997 <https://doi.org/10.5194/gmd-14-7573-2021>, 2021.
- 998 Yu, H. C., Zhang, Y. J., Nerger, L., Lemmen, C., Yu, J. C. S., Chou, T. Y., Chu, C. H., and Terng, C. T.: Development of a  
999 flexible data assimilation method in a 3D unstructured-grid ocean model under Earth System Modeling Framework,  
1000 *EGUsphere* [preprint], 2022, 1-29, <https://doi.org/10.5194/egusphere-2022-114>, 2022.
- 1001 Zhai, S. X., Jacob, D. J., Wang, X., Shen, L., Li, K., Zhang, Y. Z., Gui, K., Zhao, T. L., and Liao, H.: Fine particulate matter  
1002 (PM<sub>2.5</sub>) trends in China, 2013-2018: separating contributions from anthropogenic emissions and meteorology, *Atmos. Chem.*  
1003 *Phys.*, 19, 11031-11041, <https://doi.org/10.5194/acp-19-11031-2019>, 2019.
- 1004 Zhang, F., Wang, Z.-w., Cheng, H.-r., Lv, X.-p., Gong, W., Wang, X.-m., and Zhang, G.: Seasonal variations and chemical  
1005 characteristics of PM<sub>2.5</sub> in Wuhan, central China, *Sci. Total Environ.*, 518-519, 97-105,  
1006 <https://doi.org/10.1016/j.scitotenv.2015.02.054>, 2015.
- 1007 Zhang, J., Reid, J. S., Westphal, D. L., Baker, N. L., and Hyer, E. J.: A system for operational aerosol optical depth data  
1008 assimilation over global oceans, *J. Geophys. Res.*, 113, <https://doi.org/10.1029/2007jd009065>, 2008.



1009 Zhang, J., Campbell, J. R., Hyer, E. J., Reid, J. S., Westphal, D. L., and Johnson, R. S.: Evaluating the impact of multisensor  
1010 data assimilation on a global aerosol particle transport model, *J. Geophys. Res.-Atmos.*, 119, 4674-4689,  
1011 <https://doi.org/10.1002/2013jd020975>, 2014.  
1012